

1
2

CONNECTING OBSERVED MICROBURST PRECIPITATION WITH ITS
SCATTERING MECHANISM

3

by

Mykhaylo Sergeevich Shumko

4

A dissertation submitted in partial fulfillment
of the requirements for the degree

of

Doctor of Philosophy

in

Physics

5

MONTANA STATE UNIVERSITY
Bozeman, Montana

October 2019

6

7

©COPYRIGHT

8

by

Mykhaylo Sergeevich Shumko

2019

All Rights Reserved

DEDICATION

⁹ I dedicate this to all MSU students who use L^AT_EX. Dedication is optional
¹⁰ and may be no longer than one page, single spaced, and should precede the
¹¹ acknowledgments page.

ACKNOWLEDGEMENTS

¹² I would like acknowledge the countless engineers, technicians, and scientists who
¹³ made the FIREBIRD, AC-6, and RBSP missions a success. This work was supported
¹⁴ by Montana State University and by NASA Headquarters under the NASA Earth and
¹⁵ Space Science Fellowship Program - Grant 80NSSC18K1204. **Add co-author support.**

TABLE OF CONTENTS

16	1. INTRODUCTION	1
17	Charged Particle Motion in Electric and Magnetic Fields	2
18	Particle Populations and Their Interractions in the Magnetosphere	8
19	Inner Magnetosphere Populations.....	11
20	Plasmasphere.....	13
21	Ring Current	15
22	Radiation Belts.....	16
23	Radiation Belt Particle Sources and Sinks	20
24	Adiabatic Heating	20
25	Wave Resonance Heating	21
26	Particle Losses	23
27	Microbursts	26
28	Scope of Reserach	29
29	2. MICROBURST SCALE SIZE DERIVED FROM MULTIPLE BOUNCES 30 OF A MICROBURST SIMULTANEOUSLY OBSERVED WITH 31 THE FIREBIRD-II CUBESATS	31
32	Contribution of Authors and Co-Authors	31
33	Manuscript Information	32
34	Key Points	33
35	Introduction	35
36	Spacecraft and Observation	37
37	Analysis	40
38	Electron Bounce Period	40
39	Microburst Energy Spectra	43
40	Microburst Scale Sizes	43
41	Discussion and Conclusions	46
42	Acknowledgments	48
43	3. CONCLUSION	49
44	REFERENCES CITED	50
45	APPENDIX: Appendix A	57
46	Time and position correction	57

LIST OF FIGURES

Figure	Page
47 1.1 The three periodic motions of charged particles 48 in Earth's dipole magnetic field. These motions 49 are: gyration about the magnetic field line, bounce 50 motion between the magnetic poles, and azimuthal 51 drift around the Earth. Figure from (Baumjohann 52 and Treumann, 1997).	2
53 1.2 Charged particle motion in a uniform magnetic field 54 \vec{B} . Panel (A) shows the geometry defining the 55 pitch angle, α . Panel (B) and (C) show two helical 56 electron trajectories with dashed lines assuming a 57 large and small α (corresponding to a small and large 58 parallel velocity $v_{ }$), respectively.	6
59 1.3 Contours of constant gyration, bounce, and drift 60 frequencies for electrons and protons in a dipole field. 61 Figure from Schulz and Lanzerotti (1974).	7
62 1.4 Macroscopic structures in the outer magnetosphere. 63 The solar wind with its frozen-in interplanetary 64 magnetic field is shown on the left and is traveling 65 supersonically towards the right. The solar wind 66 envelops Earth's magnetic field to create the mag- 67 netosphere cavity. Since the solar wind is traveling 68 supersonically, it creates a bow shock up stream. 69 Downstream of the bow shock the shocked solar wind 70 plasma inside the magnetosheath flows around the 71 magnetopause, a boundary between the solar wind 72 and magnetosphere. Figure from Baumjohann and 73 Treumann (1997).	9
74 1.5 Macroscopic structures in the inner magnetosphere 75 most relevant to this dissertation. The plasmas- 76 phere, and the radiation belts are shown and ring 77 current is co-located there as well. Sun is to the left. 78 Figure from Baumjohann and Treumann (1997).	10
79 1.6 The series of steps involved in magnetic reconnection 80 with a southward IMF. Figure from Baumjohann 81 and Treumann (1997).	12

LIST OF FIGURES – CONTINUED

Figure	Page
82 1.7 Equipotential lines and electric field arrows due to 83 the superposition of the co-rotation and convection 84 electric fields. Electrons in the shaded region execute 85 closed orbits. Outside of the shaded regions the 86 electrons are not trapped and will escape. The 87 region separating the two regimes is called the Alfvén 88 layer. Figure from Baumjohann and Treumann (1997).....	14
89 1.8 The DST index during the St. Patrick's Day 2015 90 storm. This storm was caused by a coronal mass 91 ejection on March 15th, 2015. The storm phases 92 are: initial phase, main phase, and recovery phase. 93 The initial phase occurred when the Dst peaked at 94 +50 nT on March 17th during which the ring current 95 was eroded by the coronal mass ejection during the 96 interval shown by the red bar. Then the rapid 97 decrease to ≈ -200 nT was during the main phase 98 where many injections from the magnetotail pumped 99 up the ring current which reduced Earth's magnetic 100 field strength at the ground and is shown with the 101 green bar. Lastly, the recovery phase lasted from 102 March 18th to approximately March 29th during 103 which the ring current particles were lost and the 104 ring current returned to its equilibrium state. The 105 recovery phase is shown with the blue bar.....	17
106 1.9 The two radiation belts with a the locations of 107 various satelites and orbits. Figure from (Horne 108 et al., 2013).	18
109 1.10 The dynamics of the outer radiation belt in 1997 110 from the POLAR satellite. Top panel shows the 1.2- 111 2.4 MeV electron flux as a function of L and 1997 day 112 of year. The middle panel shows the DST index, and 113 bottom panel shows the solar wind velocity. Figure 114 from (Reeves et al., 2003).	19

LIST OF FIGURES – CONTINUED

Figure	Page
115 1.11 The trajectories of an electron and a right-hand circularly polarized wave during a cyclotron resonance. The electron's v_{\parallel} and the wave's k_{\parallel} are in opposite directions such that the wave's frequency is Doppler shifted to a integer multiple of the electron cyclotron frequency. Figure from (Tsurutani and Lakhina, 1997).	22
121 1.12 Various wave modes in the magnetosphere. Ultra low frequency waves occur throught the magnetosphere. Chorus waves are typically observed in the 0-12 midnight-dawn region. EMIC waves are typically observed in the dusk MLT sector. Hiss waves are observed inside the plasmasphere. Figure from Millan and Thorne (2007).	24
128 1.13 An example train of microbursts observed by FIREBIRD-II unit 4 on February 2nd, 2015. The colored curves show the differential energy channel count rates in six channels from ≈ 200 keV to greater than 1 MeV. The x-axis labels show auxiliary information such as time of observation and the spacecraft position in L, MLT, latitude and longitude coordinates.	27
135 1.14 Relativistic ($> 1\text{MeV}$) distribution of microburst occurrence rates as a function of L and MLT. The three panels show the microburst occurrence rate dependence on geomagnetic activity, parameterized by the auroral electrojet (AE) index for (a) $\text{AE} < 100$ nT, (b) $100 < \text{AE} < 300$ nT and (c) $\text{AE} > 300$ nT. Figure from Douma et al. (2017)....	28

LIST OF FIGURES – CONTINUED

Figure	Page
142 2.1 HiRes data of the microburst observed at February 143 2nd, 2015 at 06:12:53 UT, smoothed with a 150 ms 144 rolling average. The subsequent bounces showed 145 some energy dispersion. As discussed in Appendix 146 A, a time correction of -2.28 s was applied to FU3. 147 While the flux from five energy channels is shown, 148 only channels with reasonable counting statistics 149 were used for the spatial scale analysis. Vertical 150 colored bars show the \sqrt{N} error every 10th data 151 point and vertical black bars are lined up with the 152 peaks in the 220-283 keV energy channel to help 153 identify dispersion.	39
154 2.2 Observed and theoretical t_b for electrons of energies 155 from 200 to 770 keV. The solid black line is t_b 156 in a dipole magnetic field, derived in Schulz and 157 Lanzerotti (1974). The red dotted and cyan dashed 158 lines are the t_b derived using the T89, and T04 159 magnetic field models with IRBEM-Lib. Lastly, 160 the blue dot-dash curve is the t_b derived using the 161 Olson & Pfitzer Quiet model. The green and purple 162 rectangles represent the observed t_b for FU3 and 163 FU4 using a Gaussian fit, respectively. The blue 164 rectangles represent the observed t_b calculated with 165 the minima between the bounces. The width of the 166 boxes represent the width of those energy channels, 167 and the height represents the uncertainty from the fit.....	42

LIST OF FIGURES – CONTINUED

Figure	Page
168 2.3 The topology of the FIREBIRD-II orbit and the 169 multiple bounces of the microburst projected onto 170 latitude and longitude with axis scaled to equal 171 distance. Attributes relating to FU3 shown in red 172 dashed lines, and FU4 with blue solid lines. The 173 spacecraft path is shown with the diagonal lines, 174 starting at the upper right corner. The labels P1- 175 4 for FU4 and P1-5 for FU3 indicate where the 176 spacecraft were when the N^{th} peak was seen in 177 the lowest energy channel in the HiRes data. The 178 stars with the accompanying energy labels represent 179 the locations of the electrons with that energy that 180 started at time of P1, and were seen at the last peak 181 on each spacecraft. The rectangles represent the 182 lower bound of the microburst scale size, assuming 183 that the majority of the electrons were in the upper 184 boundary of energy channel 4.....	44
185 A.1 Cross-correlation time lag analysis applied to a train 186 of microbursts. Panel (a) and (b) show the count 187 rate from the lowest energy channel. Panel (c) shows 188 the cross-correlation coefficient as a function of time 189 lag. Panel (d) shows the shifted timeseries. Clock 190 difference was 2.23 s.....	59
191 A.2 Same analysis as Fig. A.1 on a different time period. 192 Clock difference was 2.21 s.....	60
193 A.3 Same analysis as Fig. A.1 on a different time period. 194 Clock difference was 2.25 s.....	61
195 A.4 Same analysis as Fig. A.1 on a different time period. 196 Clock difference was 2.27 s.....	62
197 A.5 Same cross-correlation time lag analysis applied to 198 stationary spatial structures. The cross-correlation 199 lag between these events is a sum of the clock differ- 200 ence and time lag due to the spacecraft separation. 201 The lag derived at this time was 4.95 s.....	63

LIST OF FIGURES – CONTINUED

Figure	Page
202 A.6 Same analysis as Fig. A.5 applied to a different 203 stationary spatial feature. The lag derived at this 204 time was 5.01 s.	64

NOMENCLATURE

205

- μ Dynamic viscosity
- \mathbf{n} Normal vector
- \mathbf{u} Velocity vector

INTRODUCTION

207 Above Earth's atmosphere are the a pair of Van Allen radiation belts, a complex
208 and dynamic plasma environment that effects our technology-driven society. These
209 effects include: a higher radiation dose for astronauts and cosmonauts, higher chance
210 of spacecraft failure due to single event upsets that can lead to catastrophic latchups,
211 degradation of silicon (changing the silicon doping) from an extended radiation dose
212 that can degrade a transistor to the point where it no longer function as a switch,
213 and the degradation of the ozone layer due to the chemical production of NO_X and
214 HO_X molecules. With these effects in mind, it is no surprise that the radiation belts
215 have been extensively studied since their discovery in the 1960s.

216 One natural phenomenon in the radiation belts that has been a topic of interest
217 in the space physics community is wave-particle intersections that, as we will explore
218 throughout this dissertation, can accelerate particles to very high energies (e.g. \approx
219 MeV for electrons) and scatter them into the atmosphere.

220 The goal of this dissertation is to study the wave-particle mechanism that
221 scatters microbursts, a sub-second impulse of electrons into Earth's atmosphere.
222 Before we dive deep into the physics of wave-particle interactions, an introduction to
223 Earth's magnetosphere is warranted. Single charged particle motion in Earth's electric
224 and magnetic fields will be described first. Then the major particle populations in
225 the magnetosphere and the coupling between them will be described. Lastly, a brief
226 overview of wave-particle interactions and their effects will be presented.

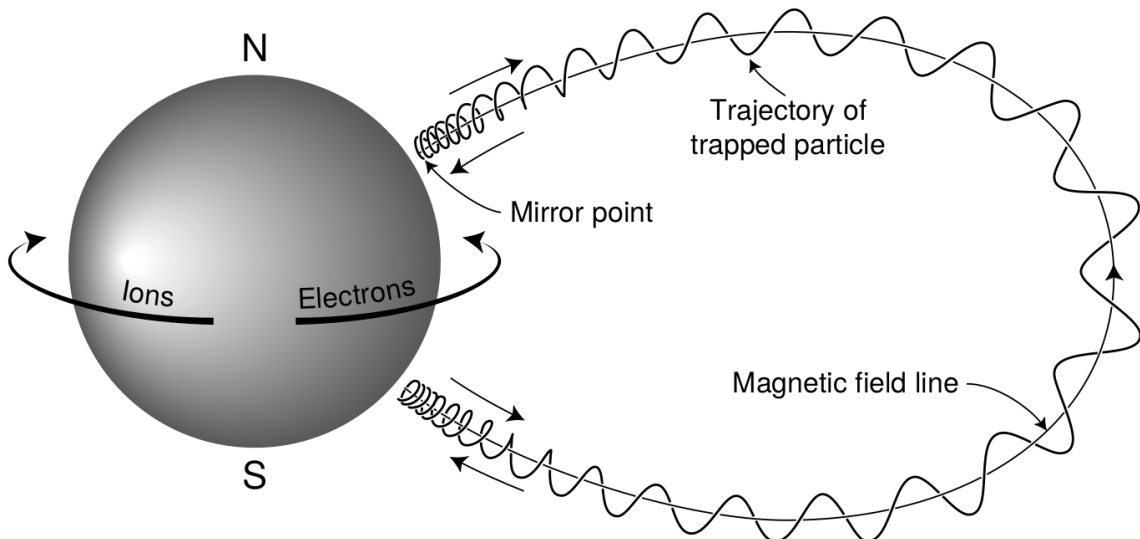


Figure 1.1: The three periodic motions of charged particles in Earth's dipole magnetic field. These motions are: gyration about the magnetic field line, bounce motion between the magnetic poles, and azimuthal drift around the Earth. Figure from (Baumjohann and Treumann, 1997).

²²⁷

Charged Particle Motion in Electric and Magnetic Fields

A charged particle trapped in the magnetosphere will experience three types of periodic motion in Earth's nearly dipolar magnetic field. The three motions are ultimately due to the Lorentz force that a particle of momentum \vec{p} , charge q , and velocity \vec{v} experiences in an electric field \vec{E} and magnetic field \vec{B} and is given by

$$\frac{d\vec{p}}{dt} = q(\vec{E} + \vec{v} \times \vec{B}). \quad (1.1)$$

- ²²⁸ In the magnetosphere, the three periodic motions in decreasing frequency are gyration,
²²⁹ bounce, and drift and are schematically shown in Fig. 1.1. Each of these
²³⁰ motions have a corresponding conserved quantity i.e. an adiabatic invariant.

The highest frequency periodic motion is gyration about a magnetic field of

magnitude B . This motion is circular with a Larmor radius of

$$r = \frac{mv_{\perp}}{|q|B} \quad (1.2)$$

where m is the mass and v_{\perp} the particle's velocity perpendicular to \vec{B} . This motion has a corresponding gyrofrequency

$$\Omega = \frac{|q|B}{m} \quad (1.3)$$

in units of radians/second. Inside the radiation belts the electron gyrofrequency, Ω_e is on the order of a kHz. The corresponding adiabatic invariant is found by integrating the particle's canonical momentum around the particle's path of gyration

$$J_i = \oint (\vec{p} + q\vec{A}) \cdot d\vec{l} \quad (1.4)$$

where J_i is the i^{th} adiabatic invariant and \vec{A} is the magnetic vector potential. This integral is carried out by integrating the first term over the circumference of the gyro orbit and integrating the second term using Stokes theorem to calculate the magnetic flux enclosed by the gyro orbit. With suitable integration, $J_1 \sim v_{\perp}^2/B$ and is conserved as the frequency of the driving force, ω satisfies $\omega \ll \Omega_e$.

The second highest frequency periodic motion is bouncing due to a parallel gradient in \vec{B} . This periodic motion naturally arises in the magnetosphere because Earth's magnetic field is stronger near the poles, and artificially in the laboratory in magnetic bottle machines. To understand this motion we first we need to define the concept of pitch angle α as the angle between \vec{B} and \vec{v} which is schematically shown in Fig. 1.2a. The pitch angle relates v with v_{\perp} , and $v_{||}$ (the component of the particles velocity parallel to \vec{B}). As shown in 1.2b and c, a larger α will tighten the

²⁴³ particle's helical trajectory and vice versa.

Assuming the particle's kinetic energy is concerned, the conservation of J_1 implies that given a particle's $v_{\perp}(0)$ and $B(0)$ at the magnetic equator (where Earth's magnetic field is usually at a minimum), we can calculate its $v_{\perp}(s)$ along the particle's path s by calculating $B(s)$ from magnetic field models. The particle's perpendicular velocity is then related via

$$\frac{v_{\perp}^2(0)}{B(0)} = \frac{v_{\perp}^2(s)}{B(s)} \quad (1.5)$$

²⁴⁴ which can be rewritten as

$$\frac{v^2 \sin^2 \alpha(0)}{B(0)} = \frac{v^2 - v_{\parallel}^2(s)}{B(s)} \quad (1.6)$$

²⁴⁵ and re-arranged to solve for $v_{\parallel}(s)$

$$v_{\parallel}(s) = v \sqrt{1 - \frac{B(s)}{B(0)} \sin^2 \alpha(0)} \quad (1.7)$$

²⁴⁶ which will tend towards 0 when the second term in the radical approaches 1.

²⁴⁷ The location where $v_{\parallel}(s) = 0$ is called the mirror point and is where a particle
²⁴⁸ stops and reverses direction. Since Earth's magnetic field is stronger towards the
²⁴⁹ poles, the mirroring particle will execute periodic bounce motion between its two
²⁵⁰ mirror points in the northern and southern hemispheres. The corresponding adiabatic
²⁵¹ invariant, J_2 is

$$J_2 = \oint p_{\parallel} ds \quad (1.8)$$

where ds describes the particle path between the mirror points in the northern and southern hemispheres (see Fig. 1.1). J_2 is found by substituting Eq. 1.7 into Eq. 1.8 and defining the magnetic field strength at the mirror points as B_m where $\alpha(m) = 90^\circ$.

The J_2 integral can be written as

$$J_2 = 2p \int_{m_n}^{m_s} \sqrt{1 - \frac{B(s)}{B(m)}} ds \quad (1.9)$$

where m_n and m_s are the northern and southern mirror points, respectively. The bounce period can be estimated (e.g. Baumjohann and Treumann, 1997) to be

$$t_b \approx \frac{LR_e}{\sqrt{W/m}} (3.7 - 1.6 \sin \alpha(0)) \quad (1.10)$$

where L is the L -shell which describes the distance from the Earth's center to the location where a particular magnetic field line crosses the magnetic equator, in units of Earth radii, R_e . W is the particle's kinetic energy. As with gyration, a particle bounces as long as $\omega \ll \Omega_b$, where Ω_b is the bounce frequency.

At this stage it is instructional to introduce the notion of the loss cone pitch angle, α_L . A particle with $\alpha \leq \alpha_L$ will mirror at or below ≈ 100 km altitude in the atmosphere. A particle at those altitudes will encounter Earth's atmosphere and has a significant probability of Coulomb scattering with atmospheric particles and be lost to the atmosphere.

The slowest periodic motion experienced by charged particles in Earth's magnetic field is azimuthal drift around the Earth. This drift results from a combination of a radial gradient in \vec{B} and the curvature of the magnetic field. The radial gradient drift arises because Earth's magnetic field is stronger near the Earth where the particle's gyroradius radius of curvature is smaller as it gyrates towards stronger magnetic field, and larger when it gyrates outward. The overall effect is the particle gyro orbit does not close on itself and negatively charged particles drift East and positively charged particles drift West. The radial gradient drift is enhanced by the centrifugal force that a particle experiences as it bounces along the curved field lines. The drift adiabatic

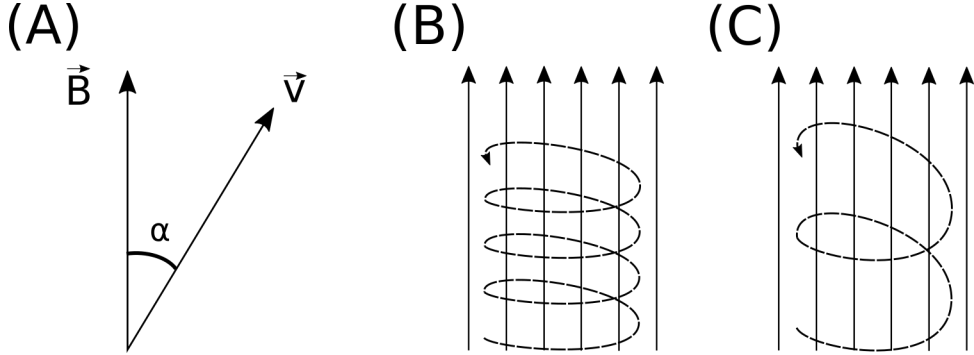


Figure 1.2: Charged particle motion in a uniform magnetic field \vec{B} . Panel (A) shows the geometry defining the pitch angle, α . Panel (B) and (C) show two helical electron trajectories with dashed lines assuming a large and small α (corresponding to a small and large parallel velocity $v_{||}$), respectively.

272 invariant, J_3 is found by integrating Eq. 1.4 over the complete particle orbit around
 273 the Earth. The shape of this drift orbit is otherwise known as a drift shell. For J_3 ,
 274 the first term is negligible and the second term is the magnetic flux enclosed by the
 275 drift shell, Φ_m i.e. $J_3 \sim \Phi_m$.

276 Figure 1.3 from Schulz and Lanzerotti (1974) shows contours of the gyration,
 277 bounce, and drift frequencies for electrons and protons in Earth's dipole magnetic
 278 field.

Up until now we have considered the three periodic motions due Earth's magnetic field and the absence of electric fields. If \vec{E} is present, a particle's center of gyration i.e., averaged position of the particle over a gyration, will drift with a velocity perpendicular to both \vec{E} and \vec{B} . The drift velocity can be solved directly from Eq. 1.1 and is

$$\vec{v}_E = \frac{\vec{E} \times \vec{B}}{B^2}. \quad (1.11)$$

279 Lastly, for more detailed derivations of these motions, see the following texts:
 280 Baumjohann and Treumann (1997); Schulz and Lanzerotti (1974); Tsurutani and
 281 Lakhina (1997).

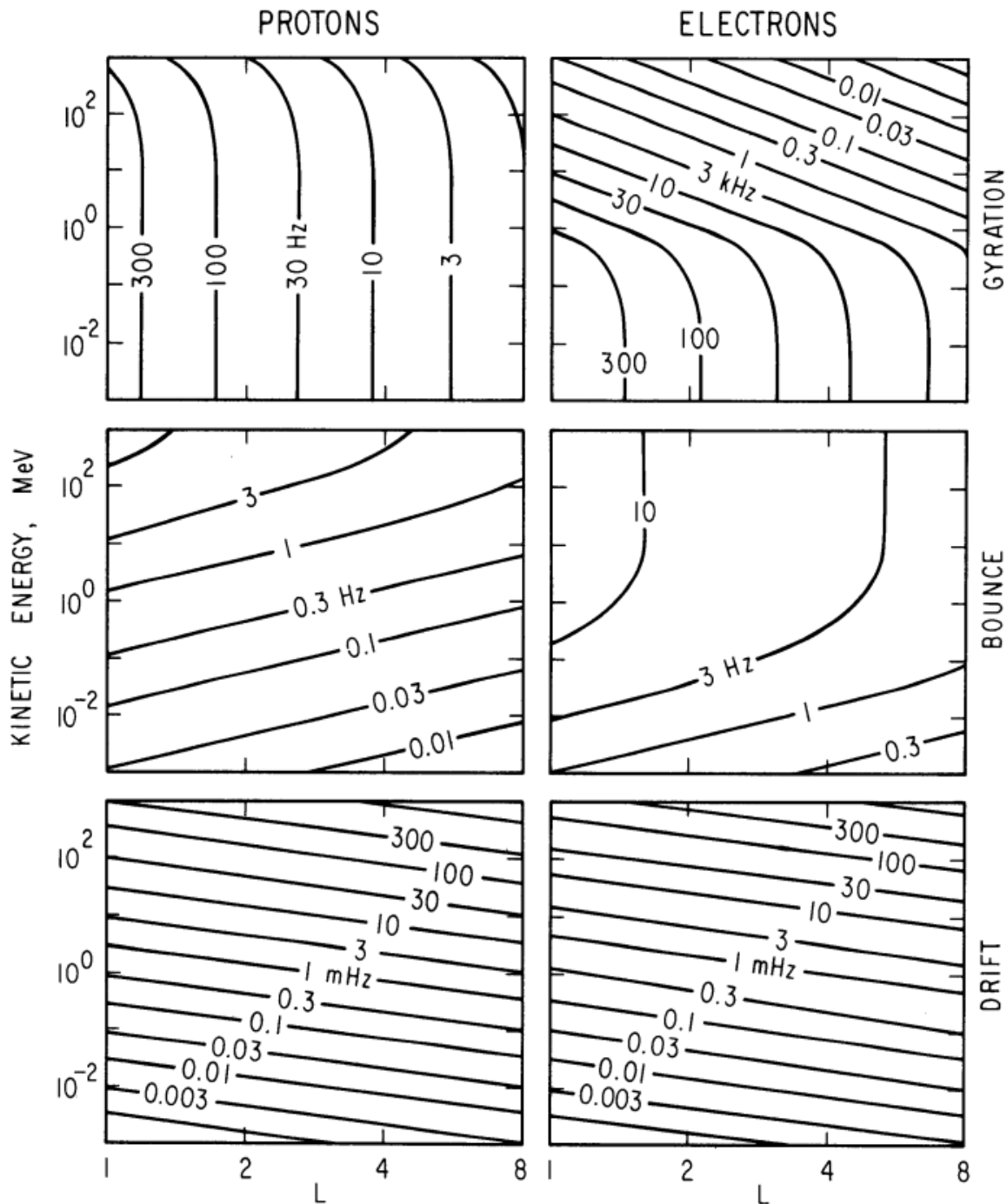


Figure 1.3: Contours of constant gyration, bounce, and drift frequencies for electrons and protons in a dipole field. Figure from Schulz and Lanzerotti (1974).

282 Particle Populations and Their Interractions in the Magnetosphere

283 The single-particle motion in Earth's magnetic field described in the previous
284 section is a prerequisite to understanding how magnetospheric particles organize into
285 macroscopic populations. The structure of the outer magnetosphere is shown in Fig.
286 1.4 and inner magnetosphere in Fig. 1.5. In this section we will introduce the various
287 particle populations in the magnetosphere and how they couple.

288 The sun and its solar wind are ultimately the source of energy input into the
289 magnetosphere. The solar wind at Earth's orbit is a plasma traveling at supersonic
290 speeds with an embedded interplanetary magnetic field (IMF). When the solar wind
291 encounters Earth's magnetic field the plasma can not easily penetrate into the
292 magnetosphere, rather it drapes around the magnetosphere forming a cavity in the
293 solar wind that is roughly shaped as shown in Fig. 1.4. Because the solar wind is
294 supersonic at 1 AU, a bow shock exists upstream of the magnetosphere. The solar
295 wind plasma, after it is shocked by the bow shock, flows around the magnetosphere
296 inside the magnetosheath. The surface where the solar wind ram pressure and Earth's
297 magnetic pressure balance is termed the magnetopause, which can be thought of as
298 a boundary between the solar wind's and Earth's plasma environments. This is
299 a slightly naive description of the magnetopause, but is nonetheless an instructive
300 conceptual picture. The shocked plasma then flows past the Earth where it shapes
301 the magnetotail. In the magnetotail the solar wind magnetic pressure balances Earth's
302 magnetic field pressure in the lobes. The magnetotail extends on the order of 100
303 R_E downstream of Earth [Add citation](#), and the tailward stretching of magnetic field
304 lines creates the plasma sheet which exists in the region of low magnetic field strength
305 near the magnetic equator [Add citation](#). The plasma sheet flows from dusk to dawn
306 (out of the page in Figs. 1.4 and 1.5) and this current is connected to a zoo of other

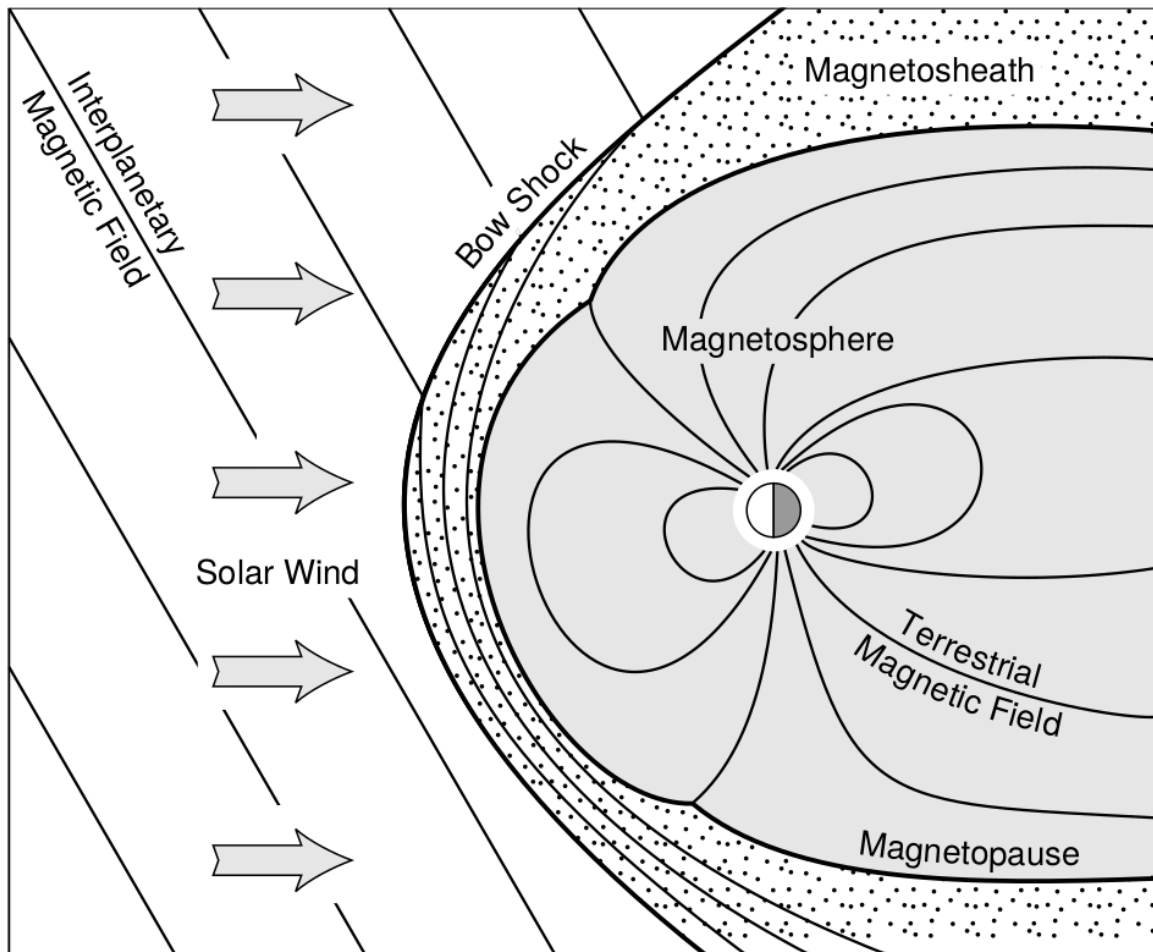


Figure 1.4: Macroscopic structures in the outer magnetosphere. The solar wind with its frozen-in interplanetary magnetic field is shown on the left and is traveling supersonically towards the right. The solar wind envelops Earth's magnetic field to create the magnetosphere cavity. Since the solar wind is traveling supersonically, it creates a bow shock up stream. Downstream of the bow shock the shocked solar wind plasma inside the magnetosheath flows around the magnetopause, a boundary between the solar wind and magnetosphere. Figure from Baumjohann and Treumann (1997).

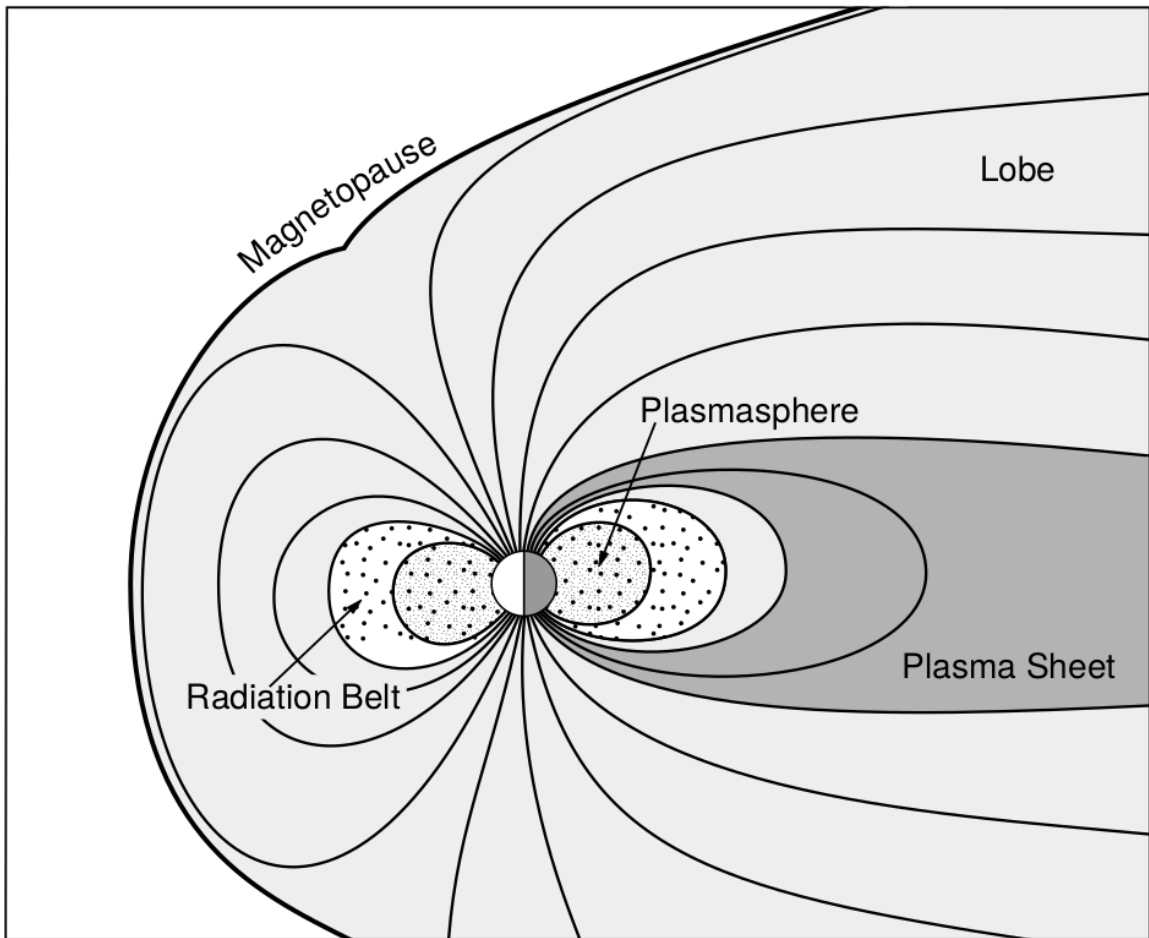


Figure 1.5: Macroscopic structures in the inner magnetosphere most relevant to this dissertation. The plasmasphere, and the radiation belts are shown and ring current is co-located there as well. Sun is to the left. Figure from Baumjohann and Treumann (1997).

307 currents in the magnetosphere which is beyond the scope of this dissertation.

308 The idea of the magnetopause as a barrier between the solar wind and
 309 the magnetosphere is not entirely accurate due to the presence of reconnection.
 310 Reconnection was first conceived by Dungey (1961) who described the convection of
 311 Earth's magnetic field between the bow and tail regions of the magnetosphere. This
 312 process is known as the Dungey cycle and is most effective when the IMF is pointing
 313 southward as is shown in Fig. 1.6 part 1. As the IMF contacts Earth's magnetic
 314 field it reconnects with it so that Earth's magnetic field is directly connected to the
 315 IMF. Then as the solar wind flows tailward the IMF drags Earth's magnetic field
 316 towards the magnetotail as shown in Fig. 1.6 parts 2-6. As more and more magnetic
 317 field lines are draped in the magnetotail, magnetic pressure increases in the lobes
 318 which squeezes the plasma sheet until Earth's magnetic field reconnects as is shown
 319 in Fig. 1.6 part 7. Lastly, Fig. 1.6 part 8 shows the newly merged magnetic field
 320 line and the plasma frozen on it moves Earthward under the magnetic tension force
 321 to become more dipolar. This is called a dipolarization of the magnetic field, and the
 322 plasma frozen on these field lines can be observed as injections (e.g. Turner et al.,
 323 2015). Injection of plasma into the inner magnetosphere is one of the drivers of inner
 324 magnetosphere dynamics. Should I talk about the K-H instability and how there
 325 could be micro reconnection? i.e. cite a paper or two that support or refute that
 326 idea.

327 Inner Magnetosphere Populations

328 Before we describe the inner magnetosphere particle populations, we first need to
 329 describe the coordinate system used to organize the inner magnetosphere populations.
 330 The first coordinate was defined in section 1 and is the L shell. L shell can be thought
 331 of as an analogue to a radius but in a dipole geometry. The azimuthal coordinate

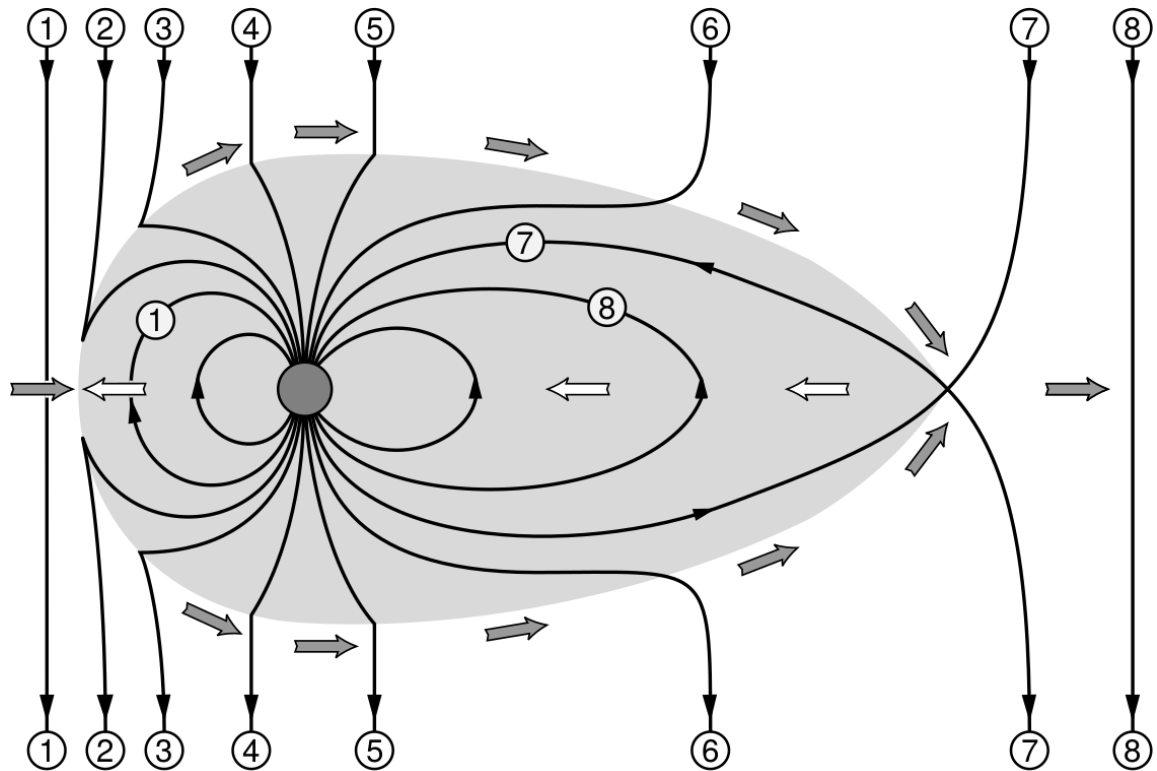


Figure 1.6: The series of steps involved in magnetic reconnection with a southward IMF. Figure from Baumjohann and Treumann (1997).

332 is the magnetic local time (MLT). For an observer above Earth's north pole looking
 333 down, MLT is defined to be 0 (midnight) in the anti-sunward direction, and increases
 334 in the counter-clockwise direction with 6 at dawn, 12 at noon (sunward direction),
 335 and 18 in dusk. The last coordinate used in this dissertation is the magnetic latitude,
 336 λ which is analogous to the latitude coordinate and is defined to be 0 at the magnetic
 337 equator.

338 The low energy particle dynamics in the inner magnetosphere are organized by
 339 two electric fields: the co-rotation and the dawn-dusk electric fields. The co-rotation
 340 electric field arises from the rotation of Earth's magnetic field. Since particles are
 341 frozen on magnetic field lines and the plasma conductivity is effectively infinite, to
 342 a non-rotating observer, Earth's rotation appears as a radial electric field that drops
 343 off as $\sim L^2$. This electric field makes particles orbit around the Earth due to the
 344 $\vec{E} \times \vec{B}$ drift. The other electric field, pointing from dawn to dusk is called the
 345 convection electric field and is formed by the Earthward transport of particles from
 346 the magnetotail that appears as an electric field to a stationary observer (with respect
 347 to Earth). The superposition of the co-rotation and convection electric fields
 348 results in a potential field shown in Fig. 1.7. The shaded area in Fig. 1.7 shows
 349 the orbits on which low energy electrons are trapped, and outside are the untrapped
 350 particles. The dynamic topology of the shaded region in Fig. 1.7 is controlled by only
 351 the convection electric field which is dependent on the solar wind speed and the IMF.
 352 The lowest energy particles, that are most effected by these electric fields, make up
 353 the plasmasphere.

354 Plasmasphere The plasmasphere is a dense ($n_e \sim 10^3/\text{cm}^3$), cool plasma
 355 ($\sim \text{eV}$) that extends to $L \sim 4$ (extent is highly dependent on the solar wind and
 356 magnetospheric conditions) and is sourced from the ionosphere. The two main

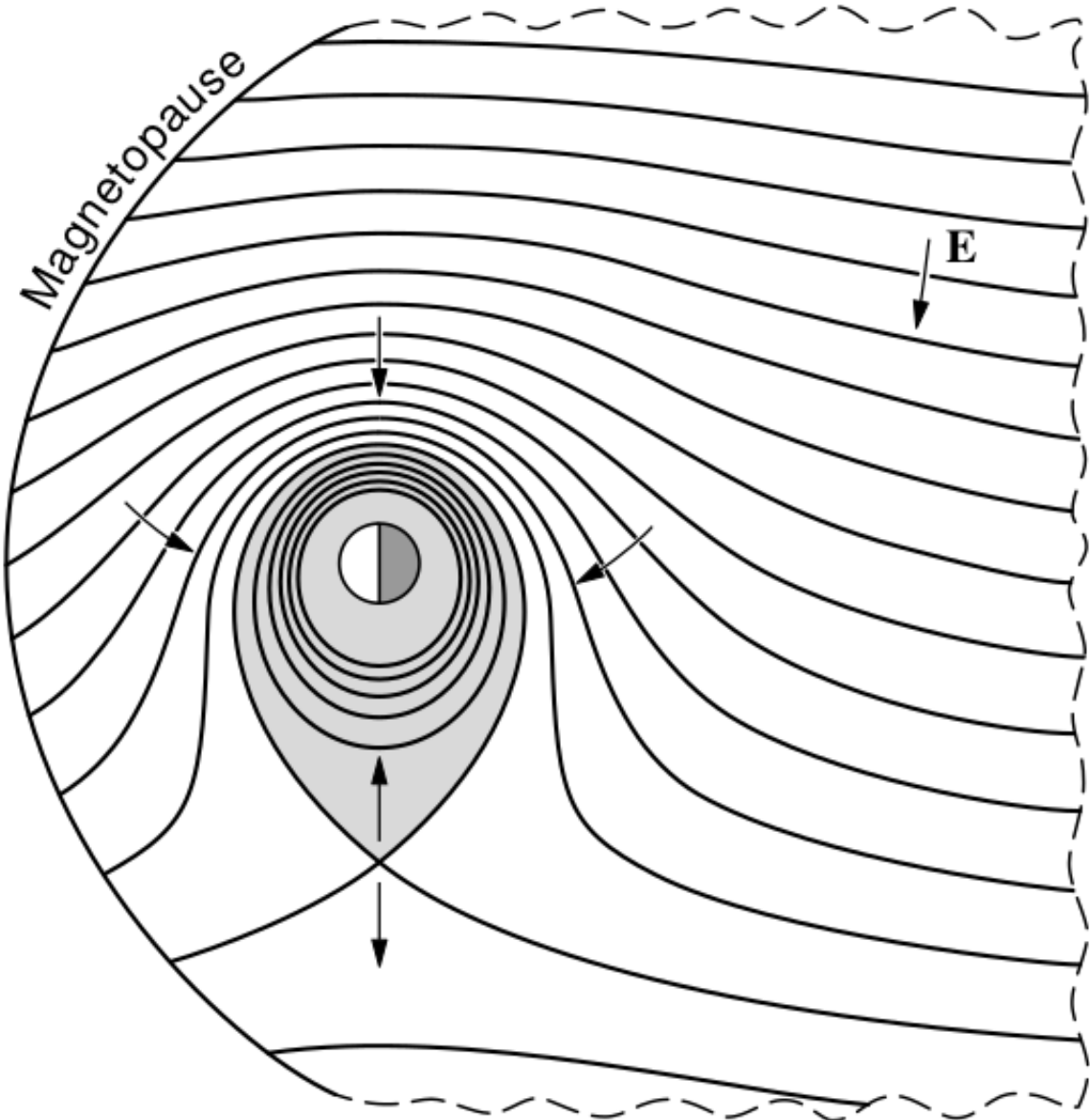


Figure 1.7: Equipotential lines and electric field arrows due to the superposition of the co-rotation and convection electric fields. Electrons in the shaded region execute closed orbits. Outside of the shaded regions the electrons are not trapped and will escape. The region separating the two regimes is called the Alfvén layer. Figure from Baumjohann and Treumann (1997).

357 mechanisms that source the cold plasma from the ionosphere are ultraviolet ionization
 358 by sunlight and particle precipitation. The ultraviolet ionization by sunlight is
 359 strongly dependent on the time of day (day vs night), latitude (more ionization near
 360 the equator). The ionization due to particle precipitation, on the other hand, is highly
 361 dependent on magnetospheric conditions, and mostly occurs at high latitudes.

362 The outer boundary of the plasmasphere is the plasmapause which is typically
 363 identified as a steep radial gradient in plasma density from $\sim 10^3/\text{cm}^3$ to $\sim 1/\text{cm}^3$. As
 364 we will see throughout this dissertation, the location of the plasmapause is important
 365 to model (e.g. O'Brien and Moldwin, 2003) and understand since the plasma density
 366 strongly controls the efficiency of particle scattering (Horne et al., 2005).

367 Ring Current The next higher energy population is the ring current. This
 368 population consists of protons and electrons between tens and a few hundred keV
 369 that drift around the Earth. The orbits of higher energy particles are not as effected
 370 by the convection and co-rotation electric field, rather they drift around the Earth
 371 due to gradient and curvature drifts. Since the direction of the drift is dependent on
 372 charge, protons drift west around the Earth and electrons drift East. This has the
 373 effect of creating a current around the Earth.

374 The ring current generates a magnetic field which decreases the magnetic field
 375 strength on Earth's surface and increases it outside of the ring current. The decrease
 376 of Earth's magnetic field strength is readily observed by a system of ground-based
 377 magnetometers and is merged into a Disturbance Storm Time (DST) index. An
 378 example of a DST index time series from a coronal mass ejection (CME) driven 2015
 379 St. Patrick's Day storm is shown in Fig. 1.8. The ring current is sometimes first
 380 depleted and DST increases slightly (initial phase or sudden storm commencement).
 381 Then the ring current is rapidly built up during which DST rapidly decreases (main

382 phase). Lastly the ring current gradually decays toward its equilibrium state over a
 383 period of a few days and DST increases towards 0 (recovery phase). The DST index
 384 along with other indicies are readily used by the space physics community to quantify
 385 the global state of the magnetosphere.

386 Radiation Belts The highest energy particle populations are in the Van Allen
 387 radiation belts. These belts were discovered by Van Allen (1959) and Vernov and
 388 Chudakov (1960) during the Cold War and are a pair of toroidally shaped populations
 389 of trapped electrons and protons usually within to $L < 8$ and are shown in Fig. 1.9.
 390 Their quiescent toroidal shape is similar to the shape of the plasmasphere and ring
 391 current and is a result of Earth's dipole magnetic field and the conservation of the
 392 three adiabatic invariants discussed in section 1.

393 The inner radiation belt is extremely stable on time periods of years, extends
 394 to $L \approx 2$, and mainly consists of protons with energies between MeV and GeV and
 395 electrons with energies up to ≈ 1 MeV (Claudepierre et al., 2019). The source of
 396 inner radiation belt protons is believed to be due to cosmic-ray albedo neutron decay
 397 (e.g. Li et al., 2017) and inward radial diffusion for electrons (e.g. O'Brien et al.,
 398 2016). The gap between the inner and outer radiation belt is called the slot, which is
 399 believed to be due to hiss waves inside the plasmasphere (described below) scattering
 400 particles into the atmosphere (e.g. Breneman et al., 2015; Lyons and Thorne, 1973).

401 The outer radiation belt, on the other hand is much more dynamic and consists
 402 of mainly electrons of energies up to a few MeV. The outer belt's spatial extent is
 403 highly variable e.g. see Fig. 1.10, and is typically observed at $4 < L < 8$. Since
 404 the outer radiation belt contains a dynamic population of energetic particles that
 405 pose a threat to human and technological presence in Earth's atmosphere and space,
 406 decades of research has been undertaken to understand and predict the outer radiation

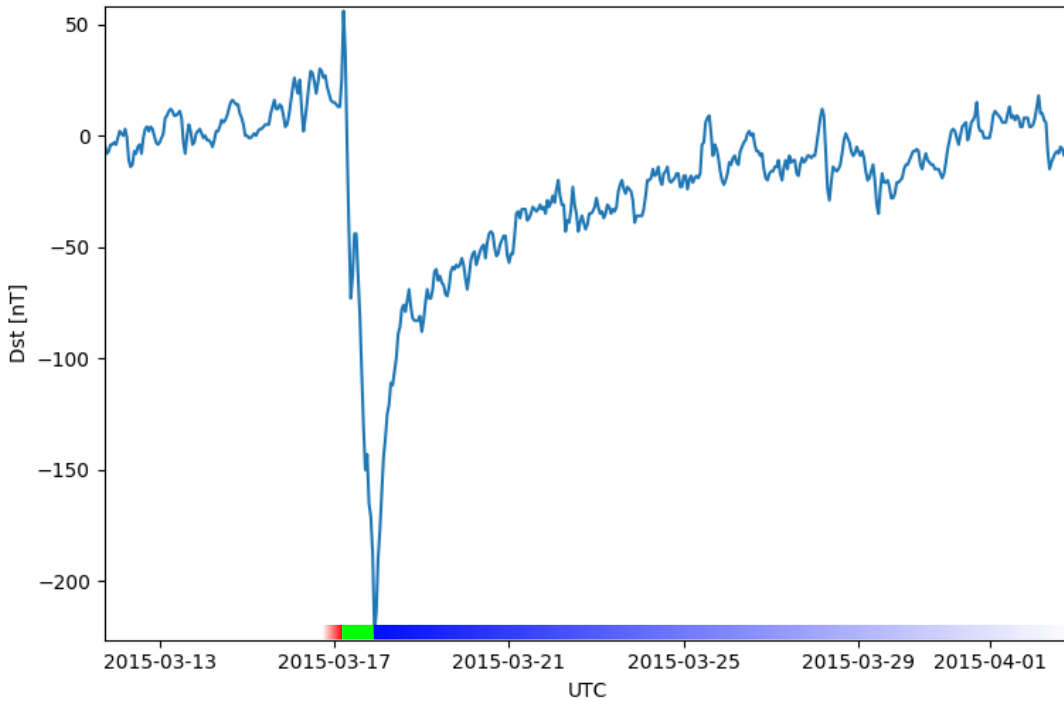


Figure 1.8: The DST index during the St. Patrick's Day 2015 storm. This storm was caused by a coronal mass ejection on March 15th, 2015. The storm phases are: initial phase, main phase, and recovery phase. The initial phase occurred when the Dst peaked at $+50$ nT on March 17th during which the ring current was eroded by the coronal mass ejection during the interval shown by the red bar. Then the rapid decrease to ≈ -200 nT was during the main phase where many injections from the magnetotail pumped up the ring current which reduced Earth's magnetic field strength at the ground and is shown with the green bar. Lastly, the recovery phase lasted from March 18th to approximately March 29th during which the ring current particles were lost and the ring current returned to its equilibrium state. The recovery phase is shown with the blue bar.

The Earth's Electron Radiation Belts

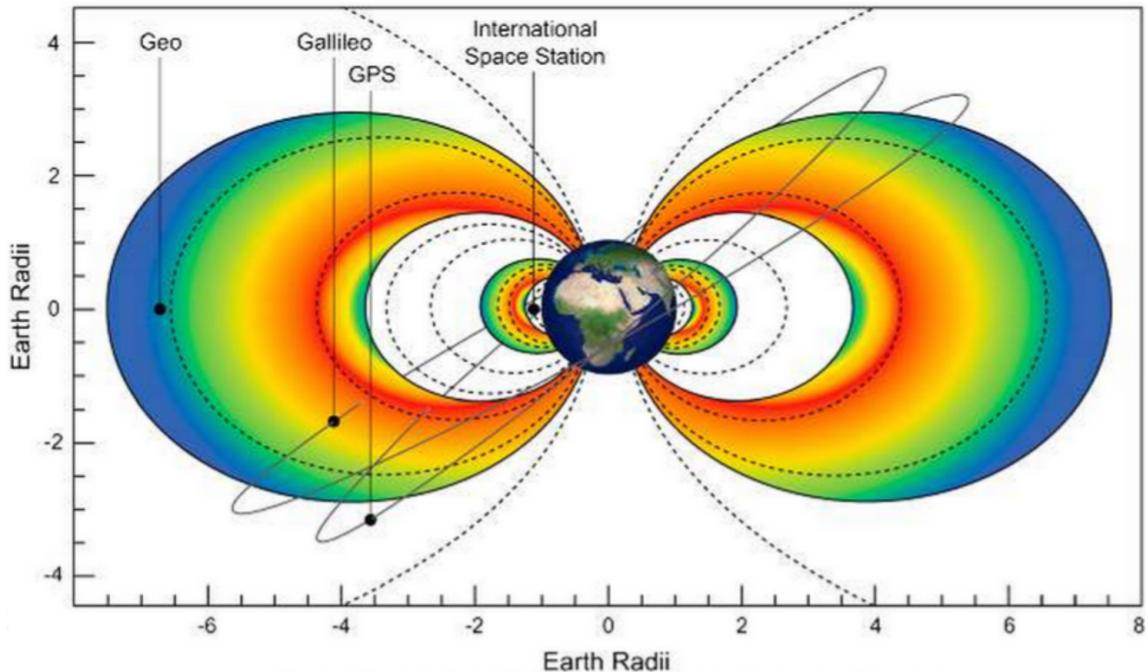


Figure 1.9: The two radiation belts with the locations of various satellites.
Figure from (Horne et al., 2013).

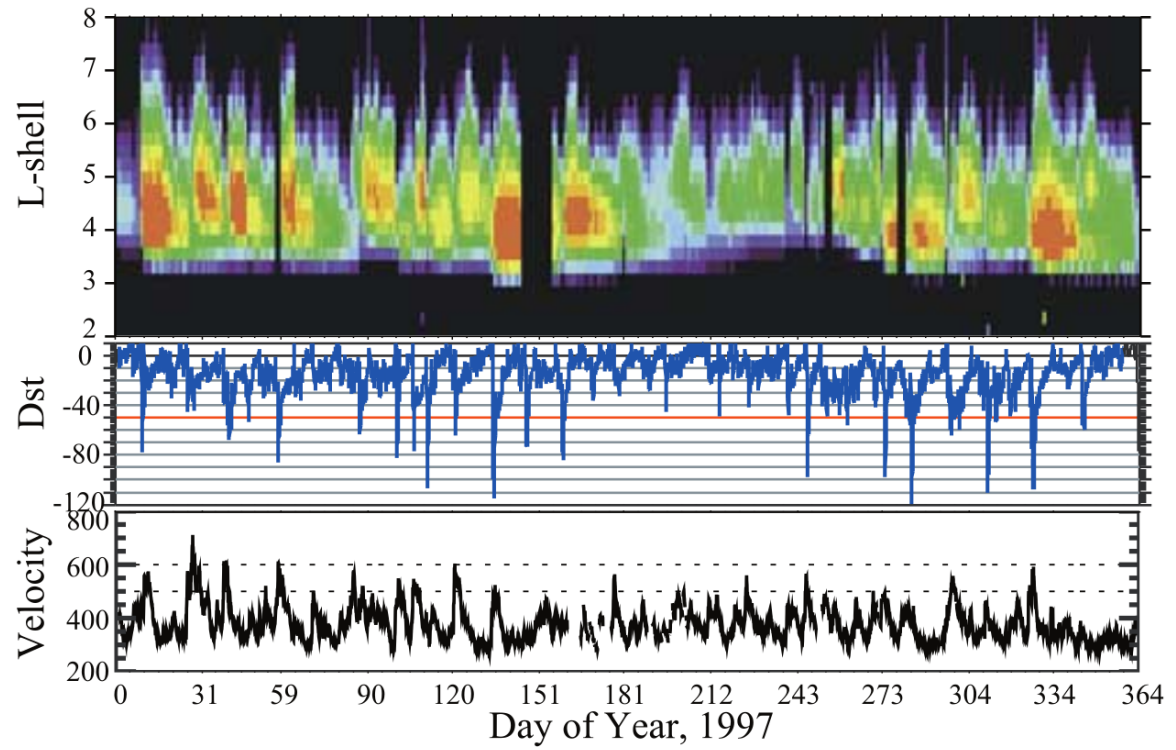


Figure 1.10: The dynamics of the outer radiation belt in 1997 from the POLAR satellite. Top panel shows the 1.2-2.4 MeV electron flux as a function of L and 1997 day of year. The middle panel shows the DST index, and bottom panel shows the solar wind velocity. Figure from (Reeves et al., 2003).

407 belt particles, waves, and wave-particle interactions. The dynamics of the outer
 408 radiation belt can be understood by considering various competing acceleration and
 409 loss mechanisms which will be described in the following sections.

410 Radiation Belt Particle Sources and Sinks

411 Adiabatic Heating

412 One of the particle heating and transport mechanisms arises from the Earthward
 413 convection of particles. The conservation of J_1 implies that the initial and final v_\perp
 414 depends on the change in the magnetic field amplitude

$$\frac{v_{\perp i}^2}{B_i} = \frac{v_{\perp f}^2}{B_f}. \quad (1.12)$$

415 As a particle convects Earthward, $B_f > B_i$ thus v_\perp must increase. The dipole
 416 magnetic field amplitude can be written as

$$B(L, \theta) = \frac{31.2 \mu\text{T}}{L^3} \sqrt{1 + 3 \cos^2 \theta} \quad (1.13)$$

417 which implies that

$$\frac{v_{\perp f}^2}{v_{\perp i}^2} = \left(\frac{L_i}{L_f} \right)^3. \quad (1.14)$$

418 .

419 In addition, as the particle convects Earthward the distance between the
 420 particle's mirror points decrease. If J_2 is conserved, the shrinking bounce path implies
 421 that $v_{||}$ must increase by

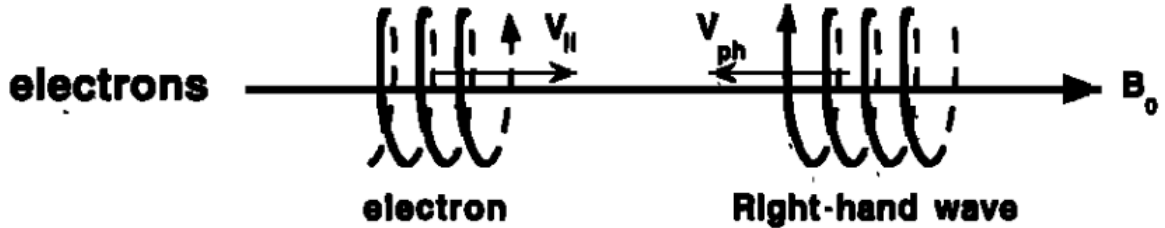
$$\frac{v_{|| f}^2}{v_{|| i}^2} = \left(\frac{L_i}{L_f} \right)^k \quad (1.15)$$

422 where k ranges from 2 for equatorial pitch angles, $\alpha_{eq} = 0^\circ$, to 2.5 for $\alpha_{eq} = 90^\circ$
 423 (Baumjohann and Treumann, 1997). Since the rate of adiabatic heating is greater in
 424 the perpendicular direction than heating in the parallel direction, an initially isotropic
 425 particle distribution will become anisotropic during its convection. These isotropic
 426 particles can then become unstable to wave growth and generate waves in order to
 427 reach equilibrium.

428 Wave Resonance Heating

429 Another mechanism that heats particles is due to particles resonating with
 430 plasma waves. A few of the electromagnetic wave modes responsible for particle
 431 acceleration (and deceleration) relevant to radiation belt dynamics are hiss, whistler
 432 mode chorus (chorus), and electromagnetic ion cyclotron (EMIC) waves. These waves
 433 are created by the loss cone instability that driven by an anisotropy of electrons
 434 for chorus waves, and protons for EMIC waves. The level of anisotropy can be
 435 quantified by the ratio of the perpendicular to parallel particle temperatures ($T_\perp/T_{||}$).
 436 A particle distribution is unstable when $T_\perp/T_{||} > 1$ which facilitates wave growth.
 437 Since electrons gyrate in a right-handed sense, the chorus waves also tend to be right
 438 hand circularly polarized (Tsurutani and Lakhina, 1997). The same argument applies
 439 to protons and left hand circularly polarized EMIC waves as well.

440 These circularly polarized waves can resonate with electrons and/or protons
 441 when their combined motion results in a static \vec{E} . One example of a resonance
 442 between a right hand circularly polarized wave and an electron is shown in Fig. 1.21
 443 and is termed the cyclotron resonance. An electron's $v_{||}$ and the wave's parallel wave
 444 vector, $k_{||}$ are in opposite directions such that the wave frequency ω is Doppler shifted
 445 to an integer multiple of the Ω_e at which point the electron feels a static electric
 446 field and is accelerated or decelerated. This acceleration happens when a resonance



$$\omega + \mathbf{k}_{\parallel} \mathbf{V}_{\parallel} = \Omega^-$$

Figure 1.11: The trajectories of an electron and a right-hand circularly polarized wave during a cyclotron resonance. The electron's v_{\parallel} and the wave's k_{\parallel} are in opposite directions such that the wave's frequency is Doppler shifted to an integer multiple of the electron cyclotron frequency. Figure from (Tsurutani and Lakhina, 1997).

⁴⁴⁷ condition is satisfied between a wave and a particle for which we will now derive an
⁴⁴⁸ illustrative toy model.

⁴⁴⁹ Assume a uniform magnetic field $\vec{B} = B_0 \hat{z}$ with a parallel propagating ($k = k \hat{z}$),
⁴⁵⁰ right-hand circularly polarized wave. The wave's electric field as a function of position
⁴⁵¹ and time can be written as

$$\vec{E} = E_0 (\cos(\omega t - kz) \hat{x} + \sin(\omega t - kz) \hat{y}) \quad (1.16)$$

which is more clearly expressed by taking the dot product to find \vec{E} in the $\hat{\theta}$ direction

$$E_{\theta} = \vec{E} \times \hat{\theta} = E_0 \cos(\omega t - kz + \theta). \quad (1.17)$$

⁴⁵² Now assume that the electron is traveling in the $-\hat{z}$ direction with a velocity $\vec{v} = -v_0 \hat{z}$
⁴⁵³ so its time dependent position along \hat{z} is

$$z(t) = -v_0 t \quad (1.18)$$

⁴⁵⁴ and gyrophase is

$$\theta(t) = -\Omega t + \theta(0) \quad (1.19)$$

⁴⁵⁵ where the first negative sign comes from the electron's negative charge. Now we put
⁴⁵⁶ this all together and express the electric field and the force that the electron will
⁴⁵⁷ experience

$$m \frac{dv_\theta}{dt} = qE_\theta = qE_0 \sin((\omega + kv_0 - \Omega)t + \theta(0)). \quad (1.20)$$

⁴⁵⁸ This is a relatively complex expression, but when the time dependent component,

$$\omega + kv_0 - \Omega = 0, \quad (1.21)$$

⁴⁵⁹ the electron will be in a static electric field which will accelerate or decelerate the
⁴⁶⁰ electron depending on θ_0 , the phase between the wave and the electron. **Show Bortnik**
⁴⁶¹ **2008 plot?** The expression in Eq. 1.21 is commonly referred to as the resonance
⁴⁶² condition and is more generally written as

$$\omega - k_{||}v_{||} = \frac{n\Omega_e}{\gamma} \quad (1.22)$$

⁴⁶³ where n is the resonance order, and γ is the relativistic correction (e.g. Millan and
⁴⁶⁴ Thorne, 2007). In the case of the cyclotron resonance, $\omega \approx \Omega_e$ thus J_1 is violated.
⁴⁶⁵ Since J_1 is violated, J_2 and J_3 are also violated since the conditions required to
⁴⁶⁶ violate J_2 and J_3 are less stringent than J_1 . It is important to remember that along
⁴⁶⁷ the particle's orbit it will encounter and experience the effects of many waves along
⁴⁶⁸ its orbit. The typical MLT extent of a handful of waves that are capable of resonating
⁴⁶⁹ with radiation belt electrons are shown in Fig. 1.12.

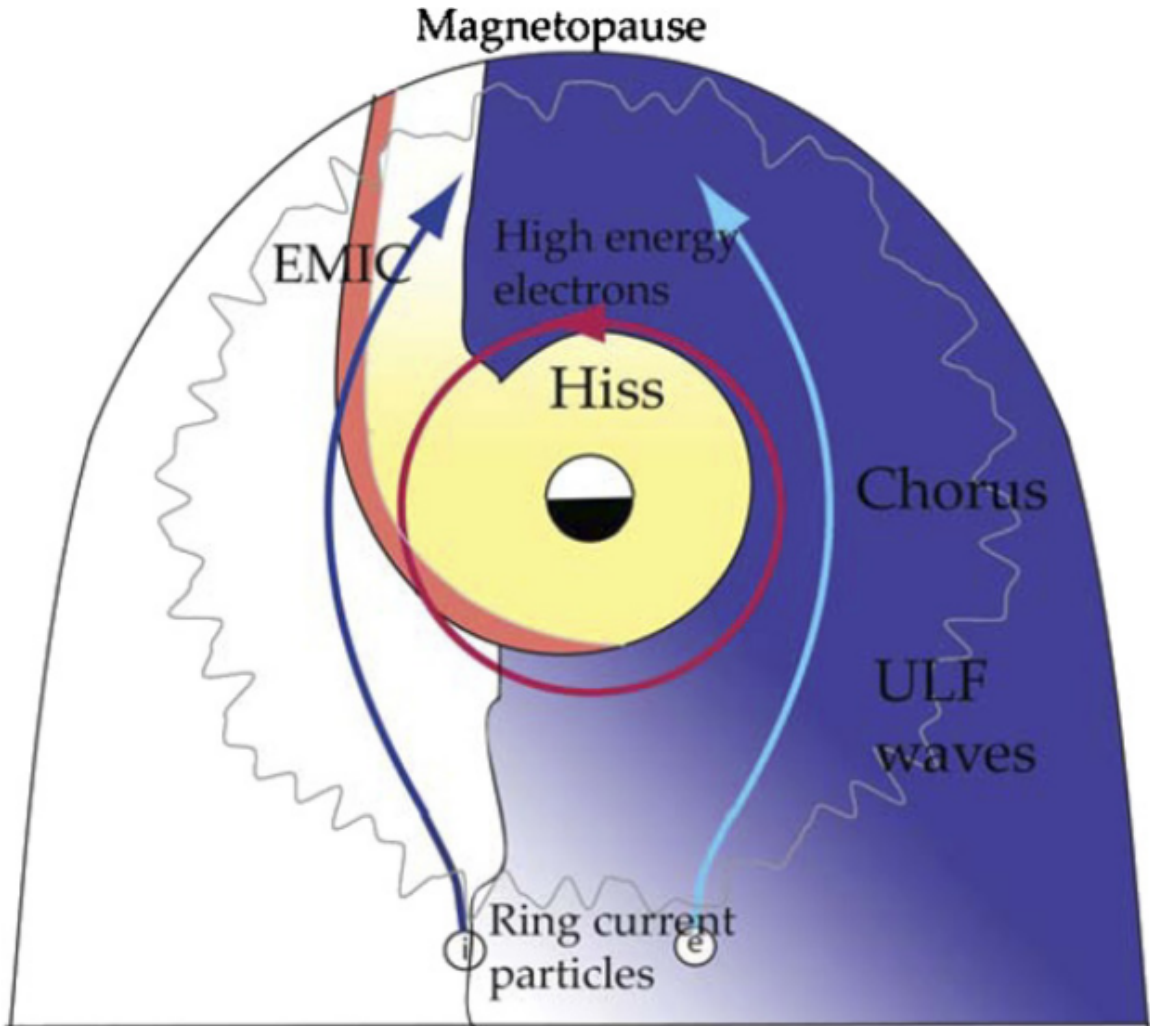


Figure 1.12: Various wave modes in the magnetosphere. Ultra low frequency waves occur through the magnetosphere. Chorus waves are typically observed in the 0-12 midnight-dawn region. EMIC waves are typically observed in the dusk MLT sector. Hiss waves are observed inside the plasmasphere. Figure from Millan and Thorne (2007).

470 Particle Losses

471 Now that we have seen two general mechanisms with which particles are
 472 accelerated and transported in the magnetosphere, we will now consider a few
 473 specific mechanisms with which particles are lost to the atmosphere or the solar
 474 wind. One particle loss mechanism into the solar wind is magnetopause shadowing
 475 (e.g. Ukhorskiy et al., 2006). Particles are sometimes lost when the ring current is
 476 strengthened and Earth's magnetic field strength is increased outside of the ring
 477 current (and reduced on Earth's surface). If the time scale of the ring current
 478 strengthening is slower than a particle drift, J_3 is conserved. Then in order to
 479 conserve J_3 while the magnetic field strength is increased, the particle's drift shell
 480 must move outward to conserve the magnetic flux contained by the drift shell. Then
 481 if the particle's drift shell expands to the point that it crosses the magnetopause, the
 482 particle will be lost to the solar wind.

483 **Move to acceleration?** Another particle loss and acceleration mechanism is driven
 484 by ultra low frequency (ULF) waves and is called radial diffusion. Radial diffusion is
 485 the transport of particles from high to low phase space density, f . If the transport is
 486 radially inward, particles will appear to be accelerated. On the other hand, radially
 487 outward radial diffusion can transport particles through the magnetopause where
 488 they will be lost to the solar wind. Reeves et al. (2013) investigated the driver of
 489 particle acceleration during the October 2012 storm and observationally found that
 490 inward radial diffusion was not dominant, rather local acceleration via wave-resonance
 491 heating (i.e. particle diffusion in pitch angle and energy which will be described below)
 492 appeared to be the dominant acceleration mechanism.

493 The loss mechanism central to this dissertation is pitch angle and energy
 494 scattering of electrons by waves. Some of the waves that scatter electrons in energy
 495 and pitch angle in the inner magnetosphere are: plasmaspheric hiss (e.g. Breneman

496 et al., 2015; O'Brien et al., 2014), EMIC waves (e.g. Capannolo et al., 2019; Hendry
 497 et al., 2017), and chorus waves (e.g. Breneman et al., 2017; Kasahara et al., 2018;
 498 Ozaki et al., 2019). These wave-particle interactions occur when the resonance
 499 condition in Eq. 1.22 is satisfied at which point the particle's energy and α is modified
 500 by the wave. More details regarding the theory of pitch angle and energy diffusion is
 501 given in Chapter X. If the wave changes α towards 0 such that $\alpha < \alpha_{LC}$, the particle's
 502 mirror point lowers to less than 100 km altitude where the particle can be lost due
 503 collisions with air. One manifestation of pitch angle scattering of particles into the
 504 loss cone are microbursts: a sub-second durtaison impulse of electrons.

505

Microbursts

506 Microbursts were first identified in high altitude balloon observations of bremsstrahlung
 507 X-rays emitted by microburst electrons impacting the atmosphere by Anderson and
 508 Milton (1964). Since then, other balloons have observed microburst X-ray signatures
 509 in the upper atmosphere (e.g. Anderson et al., 2017; Barcus et al., 1966; Brown et al.,
 510 1965; Parks, 1967; Trefall et al., 1966; Woodger et al., 2015). In addition to their X-ray
 511 signature, microbursts electrons have been directly observed in LEO with spacecraft
 512 including the Solar Anomalous and Magnetospheric Particle Explorer (SAMPEX),
 513 Focused Investigation of Relativistic Electron Bursts: Intensity, Range, and Dynamics
 514 II (FIREBIRD-II), Science Technologies Satellite (STSAT-I) (e.g. Blake et al., 1996;
 515 Blum et al., 2015; Breneman et al., 2017; Crew et al., 2016; Lee et al., 2012, 2005;
 516 Lorentzen et al., 2001a,b; Nakamura et al., 1995, 2000; O'Brien et al., 2004, 2003).
 517 An example microburst time series is shown in Fig. 1.13 and was observed by
 518 Montana State University's (MSU) FIREBIRD-II CubeSats. The prominent features
 519 of microbursts in Fig. 1.13 are their ± 1 second duration, half order of magnitude
 520 increase in count rate above the falling background, and their approximately 200-800

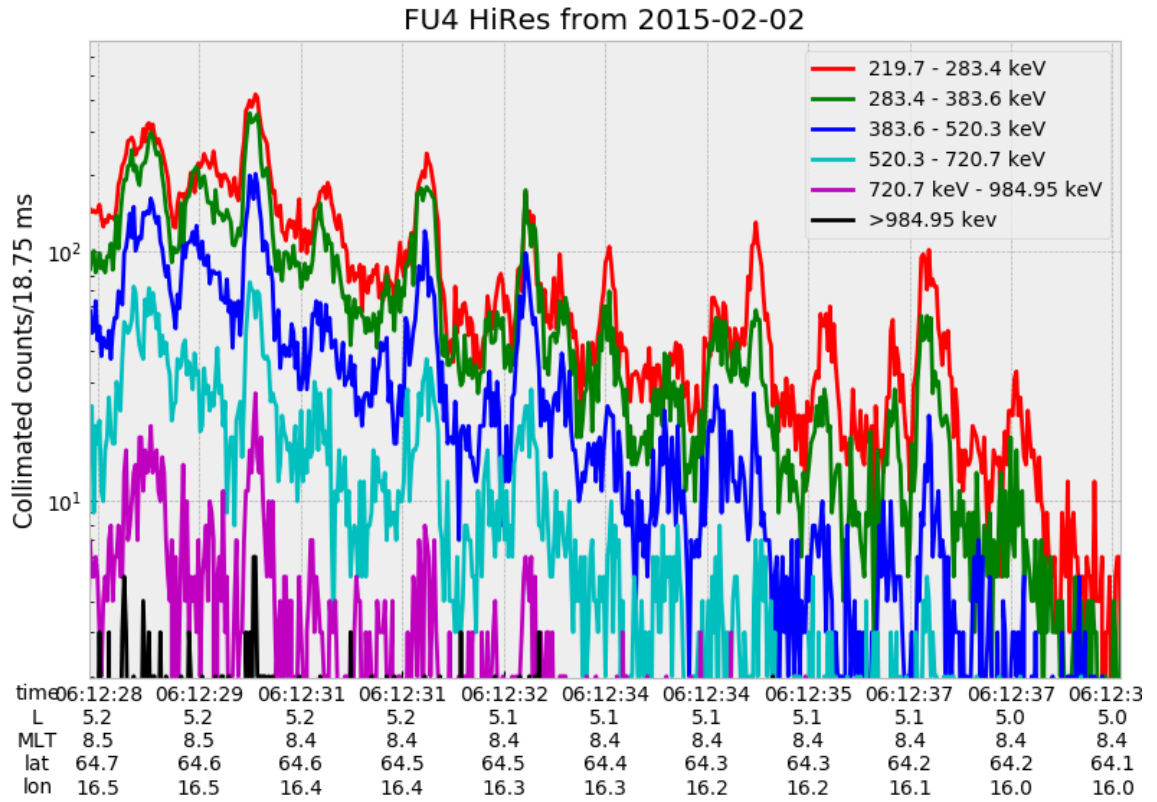


Figure 1.13: An example train of microbursts observed by FIREBIRD-II unit 4 on February 2nd, 2015. The colored curves show the differential energy channel count rates in six channels from ≈ 200 keV to greater than 1 MeV. The x-axis labels show auxiliary information such as time of observation and the spacecraft position in L, MLT, latitude and longitude coordinates.

521 keV energy extent.

522 Microbursts are observed on magnetic field footprints that are connected to the
 523 outer radiation belt (approximately $4 < L < 8$), and are predominately observed in
 524 the 0-12 MLT sector with an elevated occurrence frequency during magnetospherically
 525 disturbed times as shown in Fig. 1.14. Microbursts have been previously observed
 526 over a wide energy range from a few tens of keV (Datta et al., 1997; Parks, 1967) to
 527 greater than 1 MeV (e.g. Blake et al., 1996; Greeley et al., 2019). The microburst

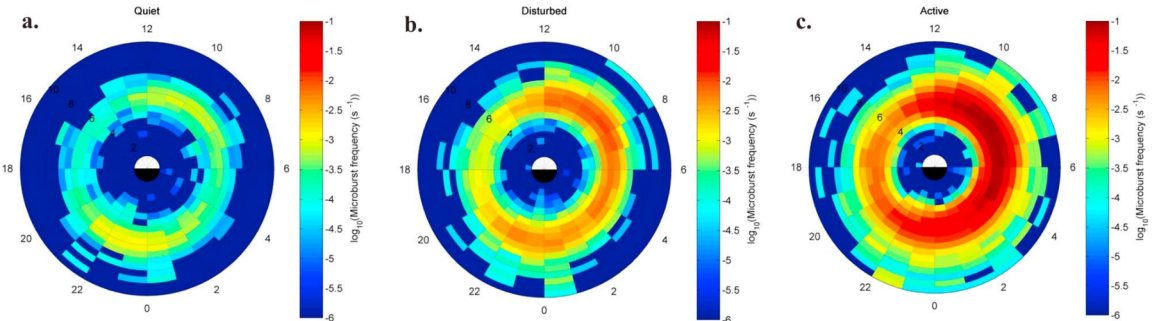


Figure 1.14: Relativistic ($> 1\text{MeV}$) distribution of microburst occurrence rates as a function of L and MLT. The three panels show the microburst occurrence rate dependence on geomagnetic activity, parameterized by the auroral electrojet (AE) index for (a) $\text{AE} < 100 \text{ nT}$, (b) $100 < \text{AE} < 300 \text{ nT}$ and (c) $\text{AE} > 300 \text{ nT}$. Figure from Douma et al. (2017).

528 electron flux (J) falls off in energy, and the microburst energy spectra is typically
 529 well fit to a decaying exponential

$$J(E) = J_0 e^{-E/E_0} \quad (1.23)$$

530 where J_0 is the flux at 0 keV (unphysical free parameter) and E_0 quantifies the
 531 efficiency of the scattering mechanism in energy (.e.g Datta et al., 1997; Lee et al.,
 532 2005; Parks, 1967). A small E_0 suggests that mostly low energy particles are scattered
 533 and a high E_0 suggests that the scattering mechanism scatters low and high energy
 534 electrons. Reality is a bit more messy and a high E_0 may be a signature of a scattering
 535 mechanism preferential to high energy electrons, but is hidden by the convolution of
 536 the source particles available to be scattered (typically with a falling energy spectrum)
 537 and the energy-dependent scattering efficiency.

538 The short duration of microbursts observed by a single LEO satellite has an
 539 ambiguity when interpreting what is exactly a microburst. The two possible realities
 540 are: a microburst is very small and spatially stationary so that the LEO spacecraft

541 passes through it in less than a second. Alternatively, microbursts are spatially large
 542 with a short duration such that the microburst passes by the spacecraft in a fraction
 543 of a second. There are a few ways to distinguish between the two possible realities,
 544 and each one has a unique set of advantages.

545 A high altitude balloon provides essentially a stationary view of the precipitating
 546 particles under the radiation belt footprints so a short-lived, temporal microburst
 547 can be unambiguously identified. Spatial structures on the other hand are difficult
 548 to identify because a balloon is essentially still on drift timescales thus a variation in
 549 the X-rays can be due to the spatial structure or an increase of precipitating particles
 550 over the whole area. Furthermore, if the stationary structure is drifting its particles
 551 are not precipitating into the atmosphere so there is no X-ray signature.

552 Another solution is multi-spacecraft missions that can determine if a microburst
 553 is spatial or temporal. As will be shown in this dissertation, if a microburst is
 554 observed simultaneously by two spacecraft then it is temporally transient and has
 555 a size greater than the spacecraft separation. On the other hand, if two spacecraft
 556 observe a microburst-like feature in the same location and at different times, then it is
 557 spatial may be a curtain (Blake and O'Brien, 2016). Both observational methods have
 558 a unique set of strengths, and this dissertation takes the multi-spacecraft approach
 559 to identify and study microbursts.

560

Scope of Research

561 This dissertation furthers our understanding of the microburst scattering
 562 mechanism by observing the scattering directly, and measuring the microburst sizes
 563 and comparing them to the size of waves near the magnetic equator where those
 564 electrons could have been scattered. Chapter X describes a microburst scattering
 565 event observed by NASA's Van Allen Probes which was studied in the theoretic

566 framework of pitch angle and energy diffusion. The following two chapters will then
567 study the size of microbursts. Chapter Y describes a bouncing packet microburst
568 observation made by MSU's FIREBIRD-II mission where the microburst's lower
569 bound longitudinal and latitudinal sizes were estimated. Then Chapter Z expands
570 the case study from Ch. Y to a statistical study of microburst sizes using The
571 Aerospace Corporation's AeroCube-6 (AC6) CubeSats. In this study, a Monte Carlo
572 and analytic microburst size models were developed to account for the compounding
573 effects of random microburst sizes and locations. Lastly, Ch. A will summarize the
574 dissertation work and make concluding remarks regarding outstanding questions in
575 microburst physics.

576 MICROBURST SCALE SIZE DERIVED FROM MULTIPLE BOUNCES OF A
577 MICROBURST SIMULTANEOUSLY OBSERVED WITH THE FIREBIRD-II
578 CUBESATS

579 Contribution of Authors and Co-Authors

580 Manuscript(s) in Chapter(s) 1

581

582 Author: [type author name here]

583 Contributions: [list contributions here, single-spaced]

584 Co-Author: [type co-author name here]

585 Contributions: [list contributions here, single-spaced]

586 Co-Author: [type co-author name here]

587 Contributions: [list contributions here, single-spaced]

588

589

Manuscript Information

590 [Type Author and Co-author(s) Names Here]

591 Geophysical Research Letters

592 Status of Manuscript: Published in a peer-reviewed journal

593 Wiley

594 Volume 45, Issue 17

595

Key Points

596

- Multiple bounces from a microburst were observed by the two FIREBIRD-II CubeSats at LEO.

598

- The lower bounds on the microburst scale size at LEO were 29 ± 1 km (latitudinal) and 51 ± 11 km (longitudinal).

600

- Deduced lower bound equatorial scale size was similar to the whistler-mode chorus source scale.

601

ABSTRACT

We present the observation of a spatially large microburst with multiple bounces made simultaneously by the FIREBIRD-II CubeSats on February 2nd, 2015. This is the first observation of a microburst with a subsequent decay made by two co-orbiting but spatially separated spacecraft. From these unique measurements, we place estimates on the lower bounds of the spatial scales as well as quantify the electron bounce periods. The microburst's lower bound latitudinal scale size was 29 ± 1 km and the longitudinal scale size was 51 ± 1 km in low earth orbit. We mapped these scale sizes to the magnetic equator and found that the radial and azimuthal scale sizes were at least 500 ± 10 km and 530 ± 10 km, respectively. These lower bound equatorial scale sizes are similar to whistler-mode chorus wave source scale sizes, which supports the hypothesis that microbursts are a product of electron scattering by chorus waves. Lastly, we estimated the bounce periods for 200-800 keV electrons and found good agreement with four common magnetic field models.

615

Introduction

616 The dynamics of radiation belt electrons are complex, and are driven by
 617 competition between source and loss processes. A few possible loss processes are
 618 radial diffusion (Shprits and Thorne, 2004), magnetopause shadowing (Ukhorskiy
 619 et al., 2006), and pitch angle and energy diffusion due to scattering of electrons by
 620 plasma waves (e.g. Abel and Thorne, 1998; Horne and Thorne, 2003; Meredith et al.,
 621 2002; Mozer et al., 2018; Selesnick et al., 2003; Summers et al., 1998; Thorne et al.,
 622 2005). There are a variety of waves that cause pitch angle scattering, including
 623 electromagnetic ion cyclotron waves, plasmaspheric hiss, and chorus (Millan and
 624 Thorne, 2007; Thorne, 2010). Chorus predominantly occurs in the dawn sector (6-
 625 12 magnetic local times (MLT)) (Li et al., 2009) where it accelerates electrons with
 626 large equatorial pitch angles and scatters electrons with small equatorial pitch angles
 627 (Horne and Thorne, 2003). Some of these electrons may be impulsively scattered
 628 into the loss cone, where they result in short-duration (~ 100 ms) enhancements in
 629 precipitating flux called microbursts.

630 Anderson and Milton (1964) coined the term microburst to describe high altitude
 631 balloon observations of ~ 100 ms duration enhancements of bremsstrahlung X-
 632 rays emitted from scattered microburst electrons impacting the atmosphere. Since
 633 then, non-relativistic (less than a few hundred keV) microbursts have been routinely
 634 observed with other balloon missions (e.g. Anderson et al., 2017; Parks, 1967; Woodger
 635 et al., 2015). A review of the literature shows no reports of microbursts above a few
 636 hundred keV observed by balloons (Millan et al., 2002; Woodger et al., 2015). This
 637 lack of observation may be explained by relatively weaker pitch angle scattering of

638 relativistic electrons by chorus (Lee et al., 2012).

639 In addition to the X-ray signature for bursts of electron precipitation, the
 640 precipitating relativistic and non-relativistic electrons have been measured in situ by
 641 spacecraft orbiting in low earth orbit (LEO). Hereinafter, we refer to these electron
 642 signatures observed by LEO spacecraft also as microbursts. Microbursts have been
 643 observed with, e.g. the Solar Anomalous and Magnetospheric Particle Explorer's
 644 (SAMPEX) \gtrsim 150 keV and \gtrsim 1 MeV channels (Blake et al., 1996; Blum et al., 2015;
 645 Lorentzen et al., 2001a,b; Nakamura et al., 1995, 2000; O'Brien et al., 2004, 2003) and
 646 Focused Investigation of Relativistic Electron Bursts: Intensity, Range, and Dynamics
 647 (FIREBIRD-II) with its \gtrsim 200 keV energy channels (Anderson et al., 2017; Breneman
 648 et al., 2017; Crew et al., 2016).

649 Understanding microburst precipitation and its scattering mechanism is impor-
 650 tant to radiation belt dynamics. The scattering mechanism has been observationally
 651 studied by e.g. Lorentzen et al. (2001b) who found that microbursts and chorus
 652 waves predominantly occur in the dawn sector and Breneman et al. (2017) made
 653 a direct observational link between individual microbursts and chorus elements.
 654 Microbursts have been modeled and empirically estimated to be capable of depleting
 655 the relativistic electron population in the outer radiation belt on the order of a day
 656 (Breneman et al., 2017; O'Brien et al., 2004; Shprits et al., 2007; Thorne et al., 2005).
 657 An important parameter in this estimation of instantaneous radiation belt electron
 658 losses due to microbursts is their scale size. Parks (1967) used balloon measurements
 659 of bremsstrahlung X-rays to estimate the high altitude scale size of predominantly low
 660 energy microbursts to be 40 ± 14 km. In Blake et al. (1996) a microburst with multiple
 661 bounces was observed by SAMPEX, and the microburst's latitudinal scale size in LEO
 662 was estimated to have been "at least a few tens of kilometers". Blake et al. (1996)
 663 concluded that typically microbursts are less than a few tens of electron gyroradii in

664 size (at $L = 5$ at LEO, the gyroradii of 1 MeV electrons is on the order of 100 m).
 665 Dietrich et al. (2010) used SAMPEX along with ground-based very low frequency
 666 stations to conclude that during one SAMPEX pass, the observed microbursts had
 667 scale sizes less than 4 km.

668 Since February 1st, 2015, microbursts have been observed by FIREBIRD-II, a
 669 pair of CubeSats in LEO. Soon after launch, when the two FIREBIRD-II spacecraft
 670 were at close range, a microburst with a scale size greater than 11 km was observed
 671 (Crew et al., 2016). On the same day, FIREBIRD-II simultaneously observed a
 672 microburst with multiple bounces. The microburst decay was observed over a period
 673 of a few seconds, while the spacecraft were traveling predominantly in latitude. Here
 674 we present the analysis and results of the latitude and longitude scale sizes and
 675 bounce periods of the first microburst with multiple bounces observed with the two
 676 FIREBIRD-II spacecraft.

677 Spacecraft and Observation

678 The FIREBIRD missions are comprised of a pair of identically-instrumented
 679 1.5U CubeSats ($15 \times 10 \times 10$ cm) that are designed to measure electron precipitation
 680 in LEO (Klumpar et al., 2015; Spence et al., 2012). The second mission, termed
 681 FIREBIRD-II, was launched on January 31st 2015. The two FIREBIRD-II CubeSats,
 682 identified as Flight Unit 3 (FU3) and Flight Unit 4 (FU4), were placed in a 632 km
 683 apogee, 433 km perigee, and 99° inclination orbit (Crew et al., 2016). FU3 and FU4
 684 are orbiting in a string of pearls configuration with FU4 ahead, to resolve the space-
 685 time ambiguity of microbursts. Each FIREBIRD-II unit has two solid state detectors:
 686 one is mounted essentially at the spacecraft surface, covered only by a thin foil acting
 687 as a sun shade, with a field of view of 90° (surface detector), and the other is beneath
 688 a collimator which restricts the field of view to 54° (collimated detector). Only FU3

689 has a functioning surface detector, so this analysis utilizes the collimated detectors.
 690 FU3's surface and collimated detectors, as well as FU4's collimated detector observe
 691 electron fluxes in six energy channels from ~ 230 keV to > 1 MeV. FIREBIRD-II's
 692 High Resolution (HiRes) electron flux data is gathered with an adjustable sampling
 693 period of 18.75 ms by default and can be as fast as 12.5 ms.

694 On February 2nd, 2015 at 06:12 UT, both FIREBIRD-II spacecraft simulta-
 695 neously observed an initial microburst, followed by subsequent periodic electron
 696 enhancements of diminishing amplitude shown in Fig. 2.1. This is thought to be
 697 the signature of a single burst of electrons, some of which precipitate, but the rest
 698 mirror near the spacecraft then bounce to the conjugate hemisphere where they mirror
 699 again and the subsequent bounces produce a train of decaying peaks (Blake et al.,
 700 1996; Thorne et al., 2005). This bounce signature occurred during the transition
 701 between the main and recovery phases of a storm with a minimum Dst of -44 nT
 702 ($K_p = 4$, and $AE \approx 400$ nT). At this time, the HiRes data was sampled at 18.75 ms.
 703 Five peaks were observed by both spacecraft. The fifth peak observed by FU4 was
 704 comparable to the Poisson noise and was not used in this analysis. This microburst
 705 was observed from the first energy channel ($\approx 200 - 300$ keV), to the fourth energy
 706 channel ($\approx 500 - 700$ keV), and FU3's surface detector observed the microburst up
 707 to the fifth energy channel (683 - 950 keV).

708 The HiRes data in Fig. 2.1 shows signs of energy dispersion, characterized by
 709 higher energy electrons arriving earlier than the lower energies. This time of flight
 710 energy dispersion tends to smear out the initial sharp burst upon each subsequent
 711 bounce. The first peak does not appear to be dispersed, and subsequent peaks show
 712 a dispersion trend consistent across energy channels. The black vertical bars have
 713 been added to Fig. 2.1 to highlight this energy dispersion. This dispersion signature
 714 and amplitude decay implies that the first peak was observed soon after the electrons

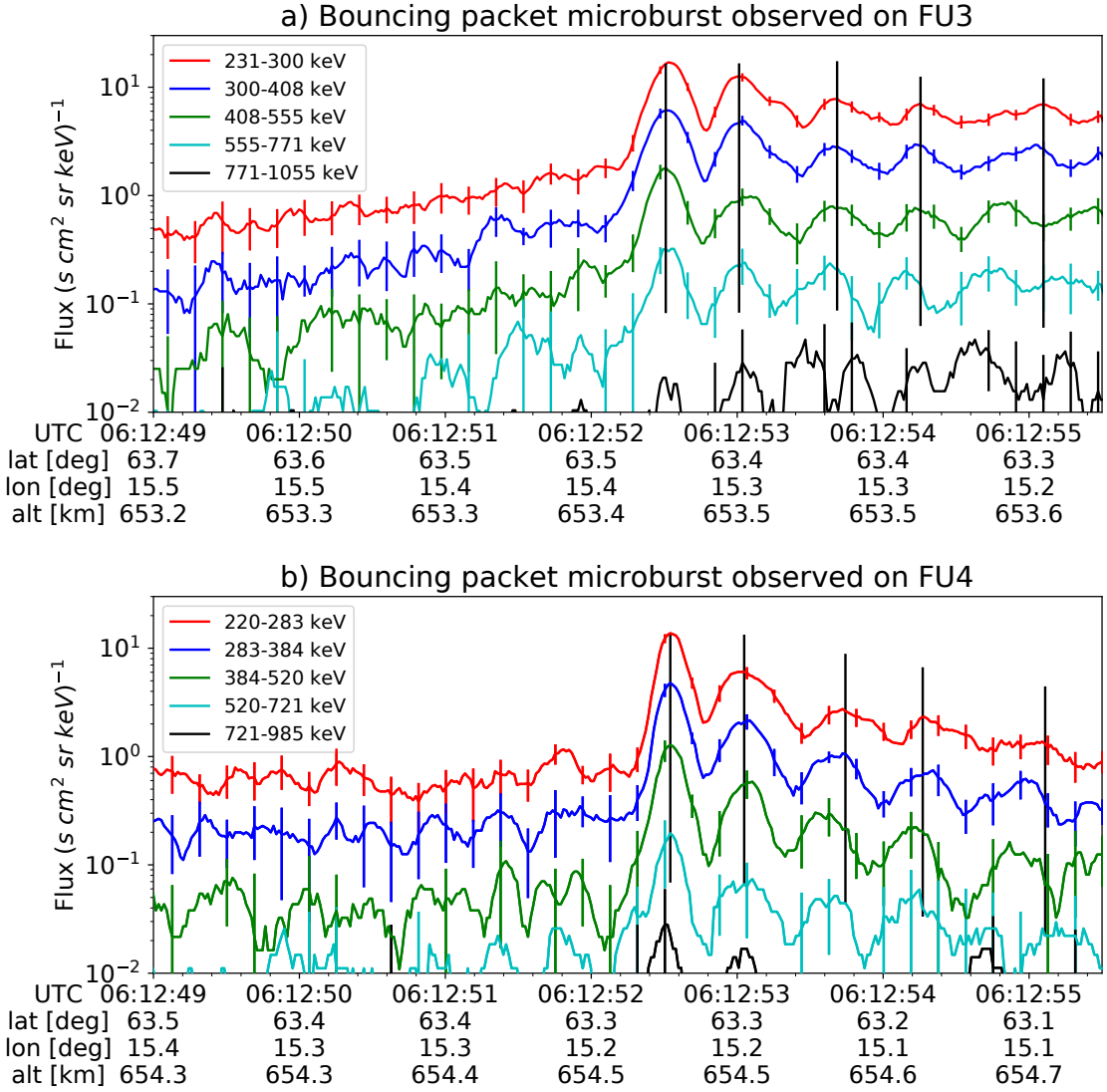


Figure 2.1: HiRes data of the microburst observed at February 2nd, 2015 at 06:12:53 UT, smoothed with a 150 ms rolling average. The subsequent bounces showed some energy dispersion. As discussed in Appendix A, a time correction of -2.28 s was applied to FU3. While the flux from five energy channels is shown, only channels with reasonable counting statistics were used for the spatial scale analysis. Vertical colored bars show the \sqrt{N} error every 10th data point and vertical black bars are lined up with the peaks in the 220-283 keV energy channel to help identify dispersion.

715 were scattered, followed by decaying bounces.

716 At this time, in magnetic coordinates, FIREBIRD-II was at McIlwain $L = 4.7$
 717 and $MLT = 8.3$, calculated with the Tsyganenko 1989 (T89) magnetic field model
 718 (Tsyganenko, 1989) using IRBEM-Lib (Boscher et al., 2012). Geographically, they
 719 were above Sweden, latitude = 63°N , longitude = 15°E , altitude = 650 km. This
 720 geographic location is magnetically conjugate to the east of the so-called South
 721 Atlantic Anomaly (SAA). The SAA is the location where the mirror points of electrons
 722 tend to occur at locations deeper in the atmosphere owing to the offset of the
 723 dipole magnetic field from the Earth's center. Electrons with pitch angles within the
 724 drift loss cone (DLC) will encounter the SAA and be removed from their eastward
 725 longitudinal drift paths (Comess et al., 2013; Dietrich et al., 2010). FU3 and FU4 are
 726 therefore both in regions where the particles in the DLC have recently precipitated,
 727 leaving only particles that were recently scattered. At the spacecraft location, locally
 728 mirroring electrons would have mirrored at 95 km in the opposite hemisphere, with
 729 more field aligned electrons mirroring at even lower altitudes. From the analysis done
 730 by Fang et al. (2010), the peak in the total ionization rate in the atmosphere for 100
 731 keV electrons is around 80 km altitude, while the total ionization rate from 1 MeV
 732 electrons peaks around 60 km altitude. It is, therefore, expected that a fraction of the
 733 microburst electrons will survive each encounter with the atmosphere. By plotting
 734 the peak flux as a function of bounce (not shown), it was found that 40 - 60 % of the
 735 microburst electrons were lost on the first bounce, similar to the 33% loss per bounce
 736 observed for a bouncing microburst observed by SAMPEX (Thorne et al., 2005).

737

Analysis

738 At the beginning of the FIREBIRD-II mission, two issues prevented the proper
 739 analysis of the microburst's spatial scale size: the spacecraft clocks were not

740 synchronized, and their relative positions were not accurately known. We addressed
 741 these issues with a cross-correlation time lag analysis described in detail in Appendix
 742 A. From this analysis, the time correction was 2.28 ± 0.12 s (applied to Fig. 2.1) and
 743 the separation was 19.9 ± 0.9 km at the time of the microburst observation.

744 Electron Bounce Period

745 We used this unique observation of bouncing electrons to calculate the bounce
 746 period, t_b as a function of energy and compare it to the energy-dependent t_b curves
 747 derived from four magnetic field models, the results of which are shown in Fig. 2.2.
 748 The observed t_b and uncertainties were calculated by fitting the baseline-subtracted
 749 HiRes flux. The baseline flux used in this analysis is given in O'Brien et al. (2004)
 750 as the flux at the 10th percentile over a specified time interval, which in this analysis
 751 was taken to be 0.5 seconds. The flux was fitted with a superposition of Gaussians
 752 for each energy channel, and the uncertainty in flux was calculated using the Poisson
 753 error from the microburst and baseline fluxes summed in quadrature. Using the fit
 754 parameters, the mean t_b for the lowest four energy channels is shown in Fig. 2.2. The
 755 trend of decreasing t_b as a function of energy is evident in Fig. 2.2, which further
 756 supports the assumption that the subsequent peaks are bounces, and not a train of
 757 microbursts scattered by bouncing chorus.

758 The decaying peaks in the 231-408 keV electron flux observed by FU3's lowest
 759 two energy channels (see Fig. 2.1) were right-skewed. One explanation is that there
 760 was in-channel energy dispersion within those channels. Since t_b of higher energy
 761 electrons is shorter, a right-skewed peak implies that higher energy electrons were
 762 more abundant within that channel e.g. in FU3's 231-300 keV channel, the 300 keV
 763 electrons will arrive sooner than the 231 keV electrons, but will they will be binned
 764 in the same channel. A Gaussian fit cannot account for this in-channel dispersion,

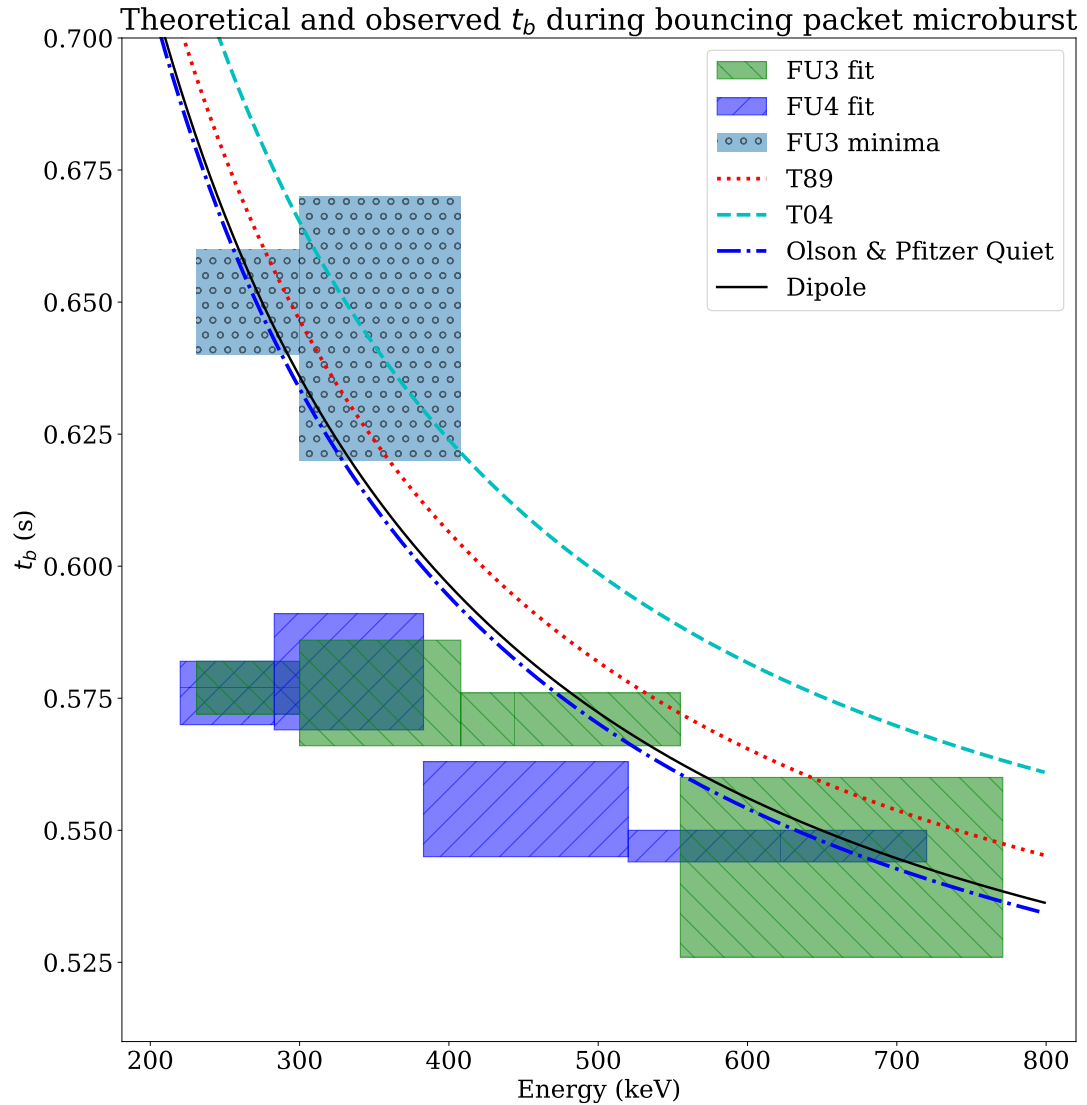


Figure 2.2: Observed and theoretical t_b for electrons of energies from 200 to 770 keV. The solid black line is t_b in a dipole magnetic field, derived in Schulz and Lanzerotti (1974). The red dotted and cyan dashed lines are the t_b derived using the T89, and T04 magnetic field models with IRBEM-Lib. Lastly, the blue dot-dash curve is the t_b derived using the Olson & Pfitzer Quiet model. The green and purple rectangles represent the observed t_b for FU3 and FU4 using a Gaussian fit, respectively. The blue rectangles represent the observed t_b calculated with the minima between the bounces. The width of the boxes represent the width of those energy channels, and the height represents the uncertainty from the fit.

and as a first order correction, minima between peaks was used to calculate t_b , and is shown in Fig. 2.2. The observed energy-dependent dispersion shown in Fig. 2.2 is consistent with higher energy peaks returning sooner. This dispersion consistency further supports the assumption that the subsequent peaks are bounces, and not a train of microbursts scattered by bouncing chorus.

To compare the observed and modeled t_b , we superposed t_b curves for various models including an analytical solution in a dipole (Schulz and Lanzerotti, 1974), and numerical models: T89, Tsyganenko 2004 (T04) (Tsyganenko and Sitnov, 2005), and Olson & Pfitzer Quiet (Olson and Pfitzer, 1982) in Fig. 2.2. The numerical t_b curves were calculated using a wrapper for IRBEM-Lib. This code traces the magnetic field line between mirror points, and calculates t_b assuming conservation of energy and the first adiabatic invariant for electrons mirroring at FIREBIRD-II. With the empirical t_b , the models agree within FIREBIRD-II's uncertainties, but the T04 model has the largest discrepancy compared to the other models.

Microburst Energy Spectra

Next, we investigated the energy spectra of this microburst. The energy spectra was modeled with an exponential that was fit to the peak flux derived from the Gaussian fit parameters in section 2 to all but the highest energy channel. We found that the E-folding energy, $E_0 \sim 100$ keV. This spectra is similar to spectra show by Lee et al. (2005) from STSAT-1 and Datta et al. (1997) from sounding rocket measurements. The energy spectra is soft for a typical microburst observed with FIREBIRD-II and there was no statistically significant change in E_0 for subsequent bounces.

788 Microburst Scale Sizes

789 Lastly, after we applied the time and separation corrections detailed in Appendix
 790 A, we mapped the locations of FU3 and FU4 in Fig. 2.3. The locations where FU3 saw
 791 peaks 1-5 and where FU4 saw peaks 1-4 are shown as P1-5 and P1-4, respectively.
 792 The lower bound on the latitudinal extent of the microburst was the difference in
 793 latitude between P1 on FU3 and P4 on FU4 and was found to be 29 ± 1 km. The
 794 uncertainty was estimated from the spacecraft separation uncertainty described in
 795 Appendix A. This scale size is the largest reported by FIREBIRD-II.

796 In section 2, we showed that the observed decaying peaks were likely due to
 797 bouncing, so we assume that the observed electrons in subsequent bounces were the
 798 drifted electrons from the initial microburst. Under this assumption, the scattered
 799 electrons observed in the last bounce by FIREBIRD-II, must have drifted east from
 800 their initial scattering longitude, allowing us to calculate the minimum longitudinal
 801 scale size. Following geometrical arguments, the distance that electrons drift east in
 802 a single bounce is a product of the circumference of the drift shell foot print, and the
 803 fraction of the total drift orbit traversed in a single bounce and is given by,

$$d_{az} = 2\pi(R_E + A) \cos(\lambda) \frac{t_b}{\langle T_d \rangle} \quad (2.1)$$

where R_E is the Earth's radius, A is the spacecraft altitude, λ is the magnetic latitude,
 t_b is the electron bounce period, and $\langle T_d \rangle$ is the electron drift period. Parks (2003)
derived $\langle T_d \rangle$ to be,

$$\langle T_d \rangle \approx \begin{cases} 43.8/(L \cdot E) & \text{if } \alpha_0 = 90^\circ \\ 62.7/(L \cdot E) & \text{if } \alpha_0 = 0^\circ \end{cases} \quad (2.2)$$

804 where E is the electron energy in MeV, L is the L shell, and α_0 is the equatorial pitch
 805 angle. Electrons mirroring at FIREBIRD-II have $\alpha_0 \approx 3.7^\circ$ and so the $\alpha_0 = 0^\circ$ limit

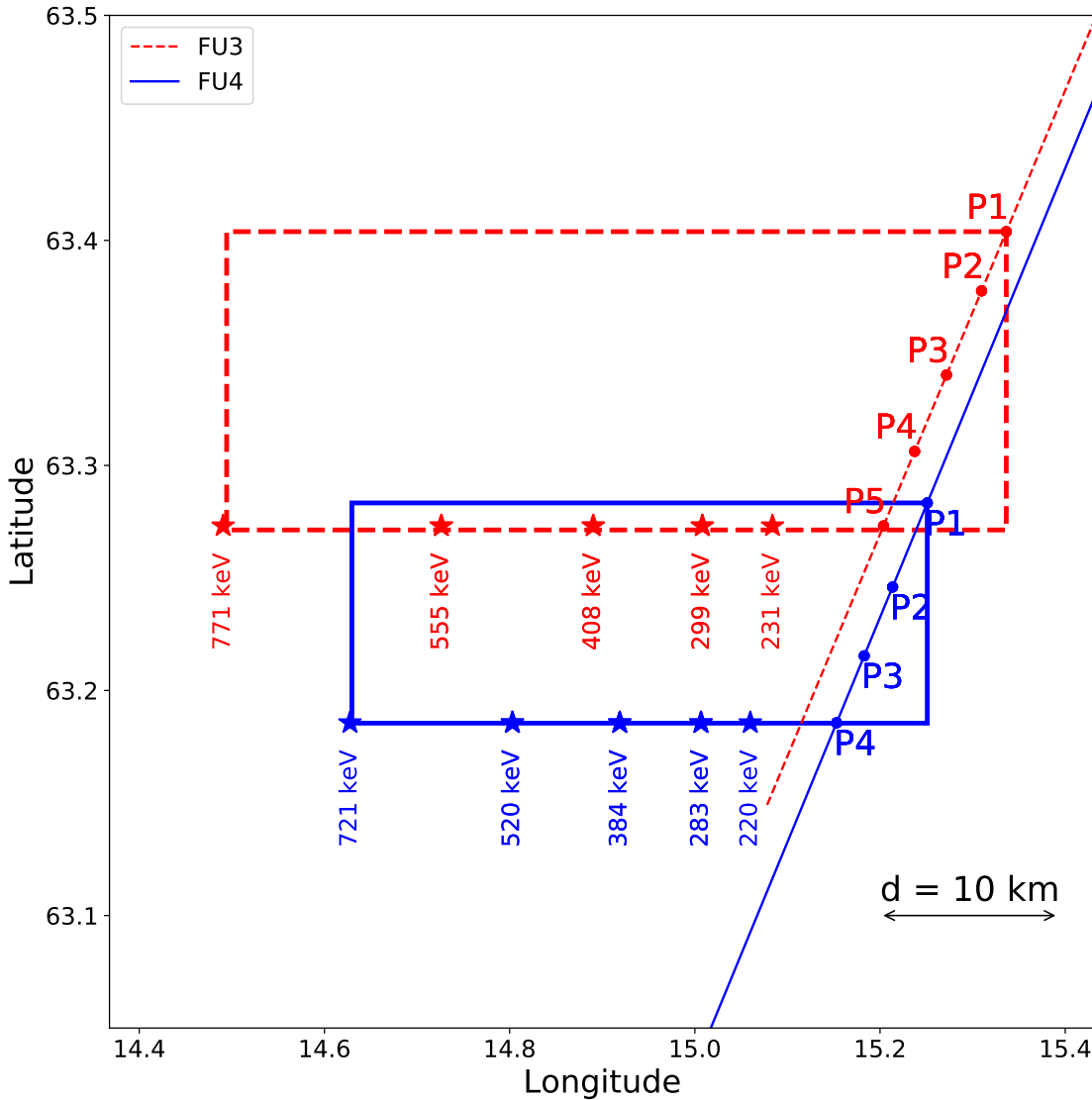


Figure 2.3: The topology of the FIREBIRD-II orbit and the multiple bounces of the microburst projected onto latitude and longitude with axis scaled to equal distance. Attributes relating to FU3 shown in red dashed lines, and FU4 with blue solid lines. The spacecraft path is shown with the diagonal lines, starting at the upper right corner. The labels P1-4 for FU4 and P1-5 for FU3 indicate where the spacecraft were when the N^{th} peak was seen in the lowest energy channel in the HiRes data. The stars with the accompanying energy labels represent the locations of the electrons with that energy that started at time of P1, and were seen at the last peak on each spacecraft. The rectangles represent the lower bound of the microburst scale size, assuming that the majority of the electrons were in the upper boundary of energy channel 4.

806 was used.

807 The microburst's longitudinal scale size is defined as the distance the highest
 808 energy electrons drifted in the time between the observations of the first and last
 809 peaks. This scale size is given by $D_{az} = n d_{az}$ where n is the number of bounces
 810 observed. The stars in Fig. 2.3 (with labels corresponding to energy channel
 811 boundaries) represent the locations when the microburst was observed at P1, such
 812 that an electron of that energy would drift eastward to be seen at P5 for FU3 and P4
 813 for FU4. Since FU3 observed more peaks it observed the larger longitudinal scale size
 814 which is shown with the red dashed box in Fig. 2.3. FU3's fourth energy channel's
 815 bounds are 555 keV and 771 keV, which correspond to longitudinal distances of 39 ± 1
 816 km and 51 ± 1 , respectively. The uncertainty was estimated by propagating the
 817 uncertainty in the bounce time Eq. 2.1. While the observed minimum longitudinal
 818 scale size is dependent on FIREBIRD-II's energy channels, the true scale size may
 819 not be.

820 To investigate how the microburst scale size compares to the scale sizes of chorus
 821 waves near the magnetic equator, the microburst's longitudinal and latitudinal scale
 822 sizes and their uncertainties in LEO were mapped to the magnetic equator with T89.
 823 The radial scale size (latitudinal scale mapped from LEO) was greater than 500 ± 10
 824 km. The azimuthal scale size (longitudinal scale mapped from LEO) of 555 keV
 825 electrons was greater than 450 ± 10 km and for the 771 keV electrons it was greater
 826 than 530 ± 10 km. The lower bound microburst scale size is similar to the chorus
 827 scale sizes derived by Agapitov et al. (2017, 2011), and is discussed below.

828

Discussion and Conclusions

829 We presented the first observation of a large microburst with multiple bounces
 830 made possible by the twin FIREBIRD-II CubeSats. The microburst's lower bound

831 LEO latitudinal and longitudinal scale sizes of 29 ± 1 km and 51 ± 1 km make
 832 it one of the largest observed. The microburst's LEO scale size was larger than
 833 the latitudinal scale sizes of typical $\gtrsim 1$ MeV microbursts reported in Blake et al.
 834 (1996), approximately 10 times larger than reported in Dietrich et al. (2010), and
 835 approximately 2.6 times larger than other simultaneous microbursts observed by
 836 FIREBIRD-II (Crew et al., 2016). Lastly, the scale sizes derived here were similar to
 837 the scale sizes of $\gtrsim 15$ keV microbursts observed with a high altitude balloon (Parks,
 838 1967). No energy dependence on the minimum latitudinal scale size was observed,
 839 while the observed energy dependence of the minimum longitudinal scale size is an
 840 artifact of the technique we used to estimate their drift motion.

841 The microburst scale size obtained in Section 2 and scaled to the geomagnetic
 842 equator can be compared with the scales of chorus waves presumably responsible for
 843 the rapid burst electron precipitation. Early direct estimates of the chorus source
 844 scales were made by the coordinated measurement by ISEE-1, 2. The wave power
 845 correlation scale was estimated to be about several hundred kilometers across the
 846 background magnetic field (Gurnett et al., 1979). Furthermore, Santolik et al. (2003)
 847 determined the correlation lengths of chorus-type whistler waves to be around 100
 848 km based on multipoint CLUSTER Wide Band Data measurements near the chorus
 849 source region at $L \approx 4$, during the magnetic storm of 18 April 2002. Agapitov et al.
 850 (2017, 2011, 2010) recently showed that the spatial extent of chorus source region can
 851 be larger, ranging from 600 km in the outer radiation belt to more than 1000 km in
 852 the outer magnetosphere. The lower bound azimuthal and latitudinal scales obtained
 853 in Section 2 and scaled to the magnetic equator, are similar to the whistler-mode
 854 chorus source scale sizes reported in Agapitov et al. (2017, 2011).

855 No wave measurements from nearby spacecraft were available at this time.
 856 Nevertheless, during the hours before and after this observation, the Van Allen Probes'

857 (Mauk et al., 2013) Electric and Magnetic Field Instrument and Integrated Science
 858 (Kletzing et al., 2013) observed strong wave power in the lower band chorus frequency
 859 range, inside the outer radiation belt between 22 and 2 MLT. Furthermore, $AE \sim 400$
 860 nT at this time, and relatively strong chorus waves were statistically more likely to
 861 be present at FIREBIRD-II's MLT (Li et al., 2009).

862 The empirically estimated and modeled t_b in this study agree within FIREBIRD-
 863 II's uncertainties, confirming that the energy-dependent dispersion was due to
 864 bouncing. The t_b curves are a proxy for field line length, and this agreement implies
 865 that they are comparable. This is expected since the magnetosphere is not drastically
 866 compressed at 8 MLT, but we expect a larger discrepancy near midnight, where the
 867 magnetosphere is more stretched and difficult to accurately model. In future studies,
 868 this analysis can be used as a diagnostic tool to validate field line lengths, and improve
 869 magnetic field models.

870 The similarity of the microburst and chorus source region scale sizes, as well
 871 as magnetospheric location and conditions, further support the causal relationship
 872 between microbursts and chorus.

873

Acknowledgments

874 This work was made possible with help from the FIREBIRD team, and the
 875 members of the Space Sciences and Engineering Laboratory at Montana State
 876 University for their hard work to make this mission a success. In addition, M.
 877 Shumko acknowledges Drew Turner for his suggestions regarding the bounce period
 878 calculations, and Dana Longcope for his proofreading feedback. The FIREBIRD-II
 879 data are available at http://solar.physics.montana.edu/FIREBIRD_II/. This analysis
 880 is supported by the National Science Foundation under Grant Numbers 0838034 and
 881 1339414. Furthermore, the work of O. Agapitov was supported by the NASA grant

882 NNX16AF85G.

CONCLUSION

884 L^AT_EX produces documents that look great, automatically handles references and
885 citations, and easily incorporates figures and tables. This is not a guide to L^AT_EX but
886 rather an introduction to the MSU style. If you want more information about L^AT_EX
887 many introductory guides can be found online.

- 889 Abel, B. and Thorne, R. M. (1998). Electron scattering loss in earth's inner
890 magnetosphere: 1. dominant physical processes. *Journal of Geophysical Research: Space Physics*, 103(A2):2385–2396.
- 892 Agapitov, O., Blum, L. W., Mozer, F. S., Bonnell, J. W., and Wygant, J. (2017).
893 Chorus whistler wave source scales as determined from multipoint van allen probe
894 measurements. *Geophysical Research Letters*, pages n/a–n/a. 2017GL072701.
- 895 Agapitov, O., Krasnoselskikh, V., Dudok de Wit, T., Khotyaintsev, Y., Pickett,
896 J. S., Santolik, O., and Rolland, G. (2011). Multispacecraft observations of chorus
897 emissions as a tool for the plasma density fluctuations' remote sensing. *Journal of Geophysical Research: Space Physics*, 116(A9):n/a–n/a. A09222.
- 899 Agapitov, O., Krasnoselskikh, V., Zaliznyak, Y., Angelopoulos, V., Le Contel, O.,
900 and Rolland, G. (2010). Chorus source region localization in the earth's outer
901 magnetosphere using themis measurements. *Annales Geophysicae*, 28(6):1377–
902 1386.
- 903 Anderson, B., Shekhar, S., Millan, R., Crew, A., Spence, H., Klumpar, D., Blake, J.,
904 O'Brien, T., and Turner, D. (2017). Spatial scale and duration of one microburst
905 region on 13 August 2015. *Journal of Geophysical Research: Space Physics*.
- 906 Anderson, K. A. and Milton, D. W. (1964). Balloon observations of X rays in the
907 auroral zone: 3. High time resolution studies. *Journal of Geophysical Research*,
908 69(21):4457–4479.
- 909 Barcus, J., Brown, R., and Rosenberg, T. (1966). Spatial and temporal character of
910 fast variations in auroral-zone x rays. *Journal of Geophysical Research*, 71(1):125–
911 141.
- 912 Baumjohann, W. and Treumann, R. A. (1997). *Basic space plasma physics*. World
913 Scientific.
- 914 Blake, J.,Looper, M., Baker, D., Nakamura, R., Klecker, B., and Hovestadt, D.
915 (1996). New high temporal and spatial resolution measurements by sampex of the
916 precipitation of relativistic electrons. *Advances in Space Research*, 18(8):171 – 186.
- 917 Blake, J. B. and O'Brien, T. P. (2016). Observations of small-scale latitudinal
918 structure in energetic electron precipitation. *Journal of Geophysical Research: Space Physics*, 121(4):3031–3035. 2015JA021815.
- 920 Blum, L., Li, X., and Denton, M. (2015). Rapid MeV electron precipitation as
921 observed by SAMPEX/HILT during high-speed stream-driven storms. *Journal of Geophysical Research: Space Physics*, 120(5):3783–3794. 2014JA020633.

- 923 Boscher, D., Bourdarie, S., O'Brien, P., Guild, T., and Shumko, M. (2012). Irbem-lib
 924 library.
- 925 Breneman, A., Crew, A., Sample, J., Klumpar, D., Johnson, A., Agapitov, O.,
 926 Shumko, M., Turner, D., Santolik, O., Wygant, J., et al. (2017). Observations
 927 directly linking relativistic electron microbursts to whistler mode chorus: Van allen
 928 probes and FIREBIRD II. *Geophysical Research Letters*.
- 929 Breneman, A. W., Halford, A., Millan, R., McCarthy, M., Fennell, J., Sample, J.,
 930 Woodger, L., Hospodarsky, G., Wygant, J. R., Cattell, C. A., et al. (2015). Global-
 931 scale coherence modulation of radiation-belt electron loss from plasmaspheric hiss.
 932 *Nature*, 523(7559):193.
- 933 Brown, R., Barcus, J., and Parsons, N. (1965). Balloon observations of auroral zone
 934 x rays in conjugate regions. 2. microbursts and pulsations. *Journal of Geophysical
 935 Research (U.S.)*.
- 936 Capannolo, L., Li, W., Ma, Q., Shen, X.-C., Zhang, X.-J., Redmon, R., Rodriguez,
 937 J., Engebretson, M., Kletzing, C., Kurth, W., et al. (2019). Energetic electron
 938 precipitation: multi-event analysis of its spatial extent during emic wave activity.
 939 *Journal of Geophysical Research: Space Physics*.
- 940 Claudepierre, S., O'Brien, T., Looper, M., Blake, J., Fennell, J., Roeder, J.,
 941 Clemmons, J., Mazur, J., Turner, D., Reeves, G., et al. (2019). A revised look
 942 at relativistic electrons in the earth's inner radiation zone and slot region. *Journal
 943 of Geophysical Research: Space Physics*, 124(2):934–951.
- 944 Comess, M., Smith, D., Selesnick, R., Millan, R., and Sample, J. (2013). Duskside
 945 relativistic electron precipitation as measured by sampex: A statistical survey.
 946 *Journal of Geophysical Research: Space Physics*, 118(8):5050–5058.
- 947 Crew, A. B., Spence, H. E., Blake, J. B., Klumpar, D. M., Larsen, B. A., O'Brien,
 948 T. P., Driscoll, S., Handley, M., Legere, J., Longworth, S., Mashburn, K.,
 949 Mosleh, E., Ryhajlo, N., Smith, S., Springer, L., and Widholm, M. (2016). First
 950 multipoint in situ observations of electron microbursts: Initial results from the
 951 NSF FIREBIRD II mission. *Journal of Geophysical Research: Space Physics*,
 952 121(6):5272–5283. 2016JA022485.
- 953 Datta, S., Skoug, R., McCarthy, M., and Parks, G. (1997). Modeling of microburst
 954 electron precipitation using pitch angle diffusion theory. *Journal of Geophysical
 955 Research: Space Physics*, 102(A8):17325–17333.
- 956 Dietrich, S., Rodger, C. J., Clilverd, M. A., Bortnik, J., and Raita, T. (2010).
 957 Relativistic microburst storm characteristics: Combined satellite and ground-based
 958 observations. *Journal of Geophysical Research: Space Physics*, 115(A12).

- 959 Douma, E., Rodger, C. J., Blum, L. W., and Clilverd, M. A. (2017). Occurrence
 960 characteristics of relativistic electron microbursts from SAMPEX observations.
 961 *Journal of Geophysical Research: Space Physics*, 122(8):8096–8107. 2017JA024067.
- 962 Dungey, J. W. (1961). Interplanetary magnetic field and the auroral zones. *Phys.
 963 Rev. Lett.*, 6:47–48.
- 964 Fang, X., Randall, C. E., Lummerzheim, D., Wang, W., Lu, G., Solomon, S. C., and
 965 Frahm, R. A. (2010). Parameterization of monoenergetic electron impact ionization.
 966 *Geophysical Research Letters*, 37(22).
- 967 Greeley, A., Kanekal, S., Baker, D., Klecker, B., and Schiller, Q. (2019). Quantifying
 968 the contribution of microbursts to global electron loss in the radiation belts. *Journal
 969 of Geophysical Research: Space Physics*.
- 970 Gurnett, D., Anderson, R., Scarf, F., Fredricks, R., and Smith, E. (1979). Initial
 971 results from the isee-1 and-2 plasma wave investigation. *Space Science Reviews*,
 972 23(1):103–122.
- 973 Hendry, A. T., Rodger, C. J., and Clilverd, M. A. (2017). Evidence of sub-mev
 974 emic-driven electron precipitation. *Geophysical Research Letters*, 44(3):1210–1218.
- 975 Hoots, F. R. and Roehrich, R. L. (1980). Models for propagation of norad element
 976 sets. Technical Report 3, Spacetrack.
- 977 Horne, R., Glauert, S., Meredith, N., Boscher, D., Maget, V., Heynderickx, D., and
 978 Pitchford, D. (2013). Space weather impacts on satellites and forecasting the earth's
 979 electron radiation belts with spacecast. *Space Weather*, 11(4):169–186.
- 980 Horne, R. B. and Thorne, R. M. (2003). Relativistic electron acceleration and
 981 precipitation during resonant interactions with whistler-mode chorus. *Geophysical
 982 Research Letters*, 30(10). 1527.
- 983 Horne, R. B., Thorne, R. M., Shprits, Y. Y., Meredith, N. P., Glauert, S. A., Smith,
 984 A. J., Kanekal, S. G., Baker, D. N., Engebretson, M. J., Posch, J. L., et al.
 985 (2005). Wave acceleration of electrons in the van allen radiation belts. *Nature*,
 986 437(7056):227.
- 987 Kasahara, S., Miyoshi, Y., Yokota, S., Mitani, T., Kasahara, Y., Matsuda, S.,
 988 Kumamoto, A., Matsuoka, A., Kazama, Y., Frey, H., et al. (2018). Pulsating
 989 aurora from electron scattering by chorus waves. *Nature*, 554(7692):337.
- 990 Kletzing, C., Kurth, W., Acuna, M., MacDowall, R., Torbert, R., Averkamp, T.,
 991 Bodet, D., Bounds, S., Chutter, M., Connerney, J., et al. (2013). The electric and
 992 magnetic field instrument suite and integrated science (EMFISIS) on RBSP. *Space
 993 Science Reviews*, 179(1-4):127–181.

- 994 Klumpar, D., Springer, L., Mosleh, E., Mashburn, K., Berardinelli, S., Gunderson,
 995 A., Handly, M., Ryhajlo, N., Spence, H., Smith, S., Legere, J., Widholm, M.,
 996 Longworth, S., Crew, A., Larsen, B., Blake, J., and Walmsley, N. (2015). Flight
 997 system technologies enabling the twin-cubesat firebird-ii scientific mission.
- 998 Lee, J. J., Parks, G. K., Lee, E., Tsurutani, B. T., Hwang, J., Cho, K. S., Kim, K.-H.,
 999 Park, Y. D., Min, K. W., and McCarthy, M. P. (2012). Anisotropic pitch angle
 1000 distribution of 100 keV microburst electrons in the loss cone: measurements from
 1001 STSAT-1. *Annales Geophysicae*, 30(11):1567–1573.
- 1002 Lee, J.-J., Parks, G. K., Min, K. W., Kim, H. J., Park, J., Hwang, J., McCarthy,
 1003 M. P., Lee, E., Ryu, K. S., Lim, J. T., Sim, E. S., Lee, H. W., Kang, K. I., and
 1004 Park, H. Y. (2005). Energy spectra of 170–360 keV electron microbursts measured
 1005 by the korean STSAT-1. *Geophysical Research Letters*, 32(13). L13106.
- 1006 Li, W., Thorne, R. M., Angelopoulos, V., Bortnik, J., Cully, C. M., Ni, B., LeContel,
 1007 O., Roux, A., Auster, U., and Magnes, W. (2009). Global distribution of whistler-
 1008 mode chorus waves observed on the THEMIS spacecraft. *Geophysical Research
 1009 Letters*, 36(9). L09104.
- 1010 Li, X., Selesnick, R., Schiller, Q., Zhang, K., Zhao, H., Baker, D. N., and Temerin,
 1011 M. A. (2017). Measurement of electrons from albedo neutron decay and neutron
 1012 density in near-earth space. *Nature*, 552(7685):382.
- 1013 Lorentzen, K. R., Blake, J. B., Inan, U. S., and Bortnik, J. (2001a). Observations
 1014 of relativistic electron microbursts in association with VLF chorus. *Journal of
 1015 Geophysical Research: Space Physics*, 106(A4):6017–6027.
- 1016 Lorentzen, K. R., Looper, M. D., and Blake, J. B. (2001b). Relativistic electron
 1017 microbursts during the GEM storms. *Geophysical Research Letters*, 28(13):2573–
 1018 2576.
- 1019 Lyons, L. R. and Thorne, R. M. (1973). Equilibrium structure of radiation belt
 1020 electrons. *Journal of Geophysical Research*, 78(13):2142–2149.
- 1021 Mauk, B., Fox, N. J., Kanekal, S., Kessel, R., Sibeck, D., and Ukhorskiy, A. (2013).
 1022 Science objectives and rationale for the radiation belt storm probes mission. *Space
 1023 Science Reviews*, 179(1-4):3–27.
- 1024 Meredith, N., Horne, R., Summers, D., Thorne, R., Iles, R., Heynderickx, D., and
 1025 Anderson, R. (2002). Evidence for acceleration of outer zone electrons to relativistic
 1026 energies by whistler mode chorus. In *Annales Geophysicae*, volume 20, pages 967–
 1027 979.
- 1028 Millan, R. and Thorne, R. (2007). Review of radiation belt relativistic electron losses.
 1029 *Journal of Atmospheric and Solar-Terrestrial Physics*, 69(3):362 – 377.

- 1030 Millan, R. M., Lin, R., Smith, D., Lorentzen, K., and McCarthy, M. (2002). X-ray observations of mev electron precipitation with a balloon-borne germanium
1031 spectrometer. *Geophysical research letters*, 29(24).
- 1033 Mozer, F. S., Agapitov, O. V., Blake, J. B., and Vasko, I. Y. (2018). Simultaneous
1034 observations of lower band chorus emissions at the equator and microburst
1035 precipitating electrons in the ionosphere. *Geophysical Research Letters*.
- 1036 Nakamura, R., Baker, D. N., Blake, J. B., Kanekal, S., Klecker, B., and Hovestadt,
1037 D. (1995). Relativistic electron precipitation enhancements near the outer edge of
1038 the radiation belt. *Geophysical Research Letters*, 22(9):1129–1132.
- 1039 Nakamura, R., Isowa, M., Kamide, Y., Baker, D., Blake, J., and Looper, M. (2000).
1040 Observations of relativistic electron microbursts in association with VLF chorus.
1041 *J. Geophys. Res.*, 105:15875–15885.
- 1042 O'Brien, T., Claudepierre, S., Blake, J., Fennell, J. F., Clemmons, J., Roeder, J.,
1043 Spence, H. E., Reeves, G., and Baker, D. (2014). An empirically observed pitch-
1044 angle diffusion eigenmode in the earth's electron belt near $l^*= 5.0$. *Geophysical*
1045 *Research Letters*, 41(2):251–258.
- 1046 O'Brien, T., Claudepierre, S., Guild, T., Fennell, J., Turner, D., Blake, J., Clemmons,
1047 J., and Roeder, J. (2016). Inner zone and slot electron radial diffusion revisited.
1048 *Geophysical Research Letters*, 43(14):7301–7310.
- 1049 O'Brien, T. and Moldwin, M. (2003). Empirical plasmapause models from magnetic
1050 indices. *Geophysical Research Letters*, 30(4).
- 1051 O'Brien, T. P., Looper, M. D., and Blake, J. B. (2004). Quantification of relativistic
1052 electron microburst losses during the GEM storms. *Geophysical Research Letters*,
1053 31(4). L04802.
- 1054 O'Brien, T. P., Lorentzen, K. R., Mann, I. R., Meredith, N. P., Blake, J. B., Fennell,
1055 J. F., Looper, M. D., Milling, D. K., and Anderson, R. R. (2003). Energization of
1056 relativistic electrons in the presence of ULF power and MeV microbursts: Evidence
1057 for dual ULF and VLF acceleration. *Journal of Geophysical Research: Space*
1058 *Physics*, 108(A8).
- 1059 Olson, W. P. and Pfitzer, K. A. (1982). A dynamic model of the magnetospheric
1060 magnetic and electric fields for july 29, 1977. *Journal of Geophysical Research:*
1061 *Space Physics*, 87(A8):5943–5948.
- 1062 Ozaki, M., Miyoshi, Y., Shiokawa, K., Hosokawa, K., Oyama, S.-i., Kataoka, R.,
1063 Ebihara, Y., Ogawa, Y., Kasahara, Y., Yagitani, S., et al. (2019). Visualization of
1064 rapid electron precipitation via chorus element wave-particle interactions. *Nature*
1065 *communications*, 10(1):257.

- 1066 Parks, G. (2003). *Physics Of Space Plasmas: An Introduction, Second Edition.*
 1067 Westview Press.
- 1068 Parks, G. K. (1967). Spatial characteristics of auroral-zone X-ray microbursts. *Journal
 1069 of Geophysical Research*, 72(1):215–226.
- 1070 Reeves, G., Spence, H. E., Henderson, M., Morley, S., Friedel, R., Funsten, H., Baker,
 1071 D., Kanekal, S., Blake, J., Fennell, J., et al. (2013). Electron acceleration in the
 1072 heart of the van allen radiation belts. *Science*, 341(6149):991–994.
- 1073 Reeves, G. D., McAdams, K. L., Friedel, R. H. W., and O'Brien, T. P. (2003). Ac-
 1074 celeration and loss of relativistic electrons during geomagnetic storms. *Geophysical
 1075 Research Letters*, 30(10):n/a–n/a. 1529.
- 1076 Santolik, O., Gurnett, D., Pickett, J., Parrot, M., and Cornilleau-Wehrlin, N. (2003).
 1077 Spatio-temporal structure of storm-time chorus. *Journal of Geophysical Research:
 1078 Space Physics*, 108(A7).
- 1079 Schulz, M. and Lanzerotti, L. J. (1974). *Particle Diffusion in the Radiation Belts.*
 1080 Springer.
- 1081 Selesnick, R. S., Blake, J. B., and Mewaldt, R. A. (2003). Atmospheric losses of
 1082 radiation belt electrons. *Journal of Geophysical Research: Space Physics*, 108(A12).
 1083 1468.
- 1084 Shprits, Y. Y., Meredith, N. P., and Thorne, R. M. (2007). Parameterization
 1085 of radiation belt electron loss timescales due to interactions with chorus waves.
 1086 *Geophysical Research Letters*, 34(11):n/a–n/a. L11110.
- 1087 Shprits, Y. Y. and Thorne, R. M. (2004). Time dependent radial diffusion modeling
 1088 of relativistic electrons with realistic loss rates. *Geophysical Research Letters*,
 1089 31(8):n/a–n/a. L08805.
- 1090 Spence, H. E., Blake, J. B., Crew, A. B., Driscoll, S., Klumpar, D. M., Larsen,
 1091 B. A., Legere, J., Longworth, S., Mosleh, E., O'Brien, T. P., Smith, S., Springer,
 1092 L., and Widholm, M. (2012). Focusing on size and energy dependence of electron
 1093 microbursts from the van allen radiation belts. *Space Weather*, 10(11).
- 1094 Summers, D., Thorne, R. M., and Xiao, F. (1998). Relativistic theory of wave-particle
 1095 resonant diffusion with application to electron acceleration in the magnetosphere.
 1096 *Journal of Geophysical Research: Space Physics*, 103(A9):20487–20500.
- 1097 Thorne, R. M. (2010). Radiation belt dynamics: The importance of wave-particle
 1098 interactions. *Geophysical Research Letters*, 37(22). L22107.

- 1099 Thorne, R. M., O'Brien, T. P., Shprits, Y. Y., Summers, D., and Horne, R. B. (2005).
 1100 Timescale for MeV electron microburst loss during geomagnetic storms. *Journal*
 1101 *of Geophysical Research: Space Physics*, 110(A9). A09202.
- 1102 Trefall, H., Bjordal, J., Ullaland, S., and Stadsnes, J. (1966). On the extension of
 1103 auroral-zone x-ray microbursts. *Journal of Atmospheric and Terrestrial Physics*,
 1104 28(2):225–233.
- 1105 Tsurutani, B. T. and Lakhina, G. S. (1997). Some basic concepts of wave-particle
 1106 interactions in collisionless plasmas. *Reviews of Geophysics*, 35(4):491–501.
- 1107 Tsyganenko, N. (1989). A solution of the chapman-ferraro problem for an ellipsoidal
 1108 magnetopause. *Planetary and Space Science*, 37(9):1037 – 1046.
- 1109 Tsyganenko, N. A. and Sitnov, M. I. (2005). Modeling the dynamics of the inner
 1110 magnetosphere during strong geomagnetic storms. *Journal of Geophysical Research:*
 1111 *Space Physics*, 110(A3).
- 1112 Turner, D., Claudepierre, S., Fennell, J., O'Brien, T., Blake, J., Lemon, C.,
 1113 Gkioulidou, M., Takahashi, K., Reeves, G., Thaller, S., et al. (2015). Energetic
 1114 electron injections deep into the inner magnetosphere associated with substorm
 1115 activity. *Geophysical Research Letters*, 42(7):2079–2087.
- 1116 Ukhorskiy, A. Y., Anderson, B. J., Brandt, P. C., and Tsyganenko, N. A. (2006).
 1117 Storm time evolution of the outer radiation belt: Transport and losses. *Journal of*
 1118 *Geophysical Research: Space Physics*, 111(A11):n/a–n/a. A11S03.
- 1119 Van Allen, J. A. (1959). The geomagnetically trapped corpuscular radiation. *Journal*
 1120 *of Geophysical Research*, 64(11):1683–1689.
- 1121 Vernov, S. and Chudakov, A. (1960). Investigation of radiation in outer space. In
 1122 *International Cosmic Ray Conference*, volume 3, page 19.
- 1123 Woodger, L., Halford, A., Millan, R., McCarthy, M., Smith, D., Bowers, G., Sample,
 1124 J., Anderson, B., and Liang, X. (2015). A summary of the BARREL campaigns:
 1125 Technique for studying electron precipitation. *Journal of Geophysical Research:*
 1126 *Space Physics*, 120(6):4922–4935.

1127

APPENDIX: APPENDIX A

1128 This appendix describes the method we used to calculate the time difference and
 1129 separation between FU3 and FU4 at 06:12 UT on February 2nd, 2015.

1130

Time and position correction

1131 We used the following method to calculate the clock difference, δt_c and
 1132 separation, d between FU3 and FU4 at 06:12 UT on February 2nd, 2015.

1133 The relative clock difference was calculated with a cross-correlation time
 1134 lag analysis on uniquely-identified trains of microbursts that hit both spacecraft
 1135 simultaneously. Four time periods with coincident microbursts were hand-picked on
 1136 February 2nd, 2015 and are shown in Figs. A.1-A.4, panels (a) and (b). The cross-
 1137 correlation time lag analysis was applied to the HiRes time series in panels (a) and
 1138 (b), and the resulting normalized cross-correlation coefficient as a function of time is
 1139 shown in panel (c). To validate the peak lag identified in panel (c), FU3's time series
 1140 was shifted by that lag and is shown in panel (d).

1141 The clock differences from the simultaneous microbursts in Figs. A.1-A.4 were
 1142 linearly fit to account for the relative clock drift (≈ 20 ms/hour at this time), giving
 1143 a value of $\delta t_c = 2.28 \pm 0.12$ s at the time of the microburst analyzed here. This time
 1144 shift was applied to the HiRes data in Fig. 1. A clock difference of $\delta t_c = 2.45^{+0.51}_{-0.98}$ s
 1145 was independently calculated with the FIREBIRD-II telemetry beacon time stamps
 1146 that were downlinked during operational passes.

1147 We calculate the spacecraft separation, by applying same the cross-correlation
 1148 time lag analysis on structures assumed to be spatial and are shown in Figs. A.5
 1149 and A.6. The lag from the peak cross-correlation between these events is a sum of
 1150 the clock difference and time lag due to the spacecraft separation. We interpret the
 1151 time lag due to the spacecraft separation as the time difference between when the
 1152 leading satellite observed a stationary spatial feature, to when the trailing satellite
 1153 observed the same stationary spatial feature. With the method described above, we
 1154 find the spatial time lag to be $\delta t_d = 2.64 \pm 0.12$ s (after we account for the clock
 1155 difference and its uncertainty). To convert from a spatial time lag to a spacecraft
 1156 separation, we calculate the satellite velocity. We calculate the velocity using a Two
 1157 Line Element (TLE), a data format containing the orbit parameters that are used
 1158 for orbit propagation. With the TLE derived spacecraft velocity, $v = 7.57$ km/s, the
 1159 spacecraft separation was $d = 19.9 \pm 0.9$ km.

1160 An independent method to calculate the spacecraft separation was developed.
 1161 The separation was calculated using TLEs. The TLE from February 2nd was
 1162 anomalous and was not used in this analysis. Instead, seven TLEs released up to
 1163 five days after the microburst event were backpropagated, using the SGP-4 algorithm

1164 (Hoots and Roehrich, 1980) that calculates orbital state vectors with perturbations
1165 such as Earth's atmosphere, as well as gravitational effects from the moon and sun.
1166 Then the predicted spacecraft separations at the time of the microburst event were
1167 averaged to derive a separation of $d = 18.4 \pm 1.5$ km. These two methods give
1168 similar separations, which implies that the stationary event assumption used in the
1169 cross-correlation time lag analysis is reasonable.

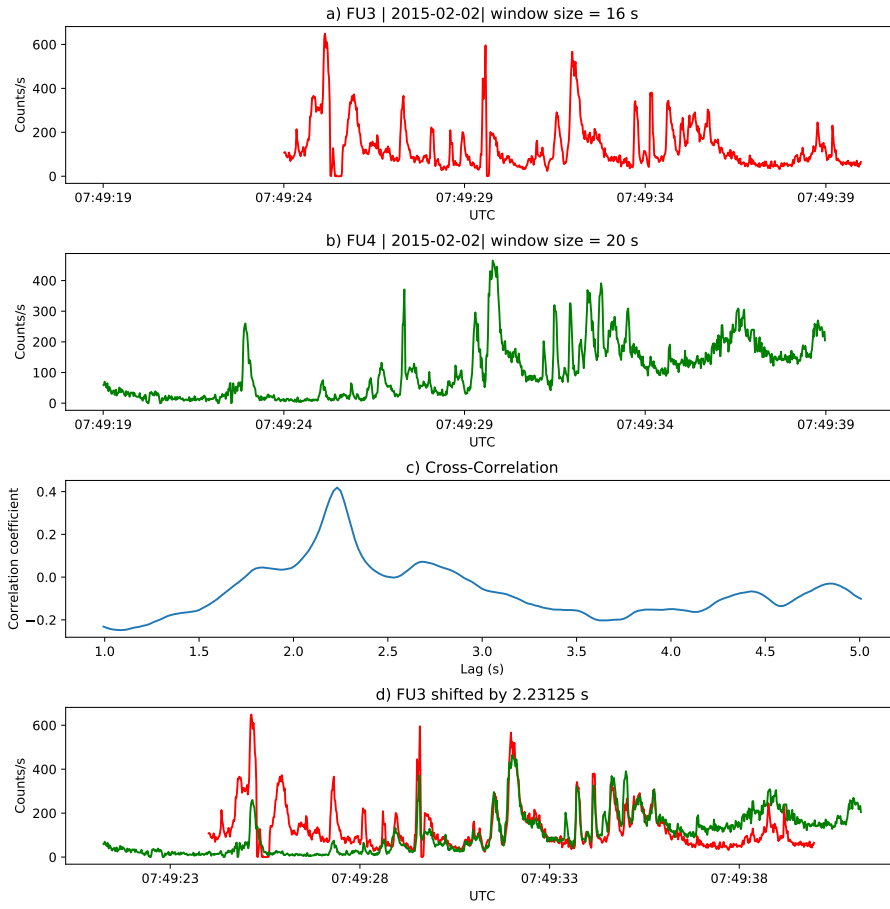


Figure A.1: Cross-correlation time lag analysis applied to a train of microbursts. Panel (a) and (b) show the count rate from the lowest energy channel. Panel (c) shows the cross-correlation coefficient as a function of time lag. Panel (d) shows the shifted timeseries. Clock difference was 2.23 s.

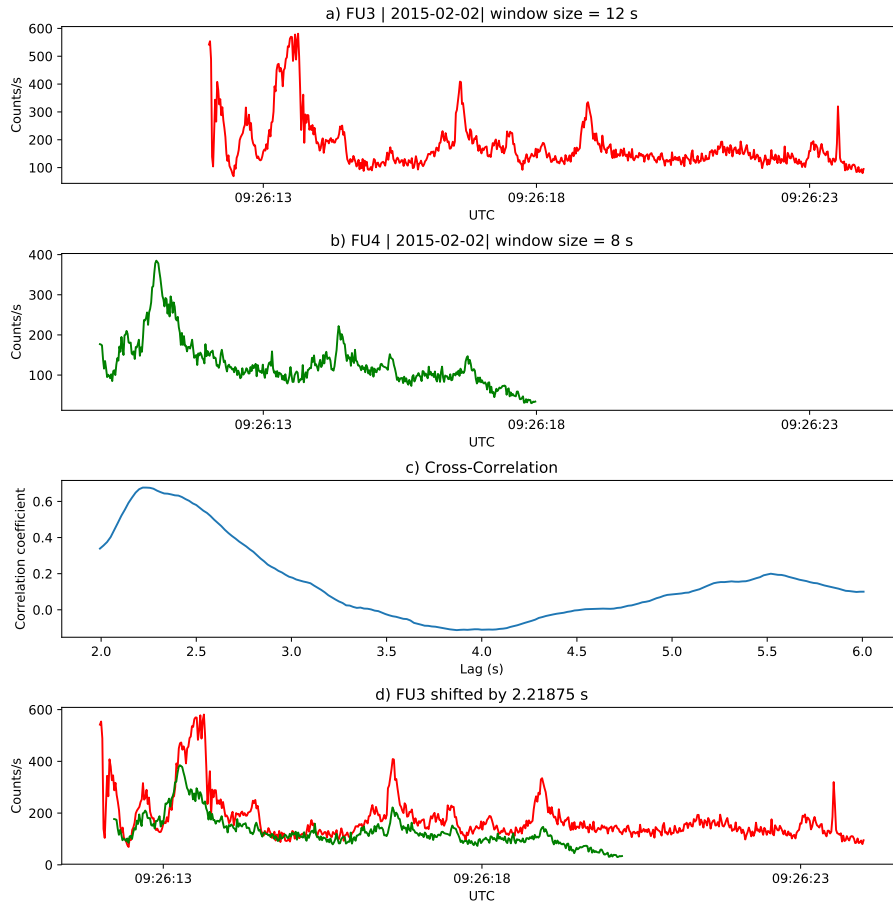


Figure A.2: Same analysis as Fig. A.1 on a different time period. Clock difference was 2.21 s.

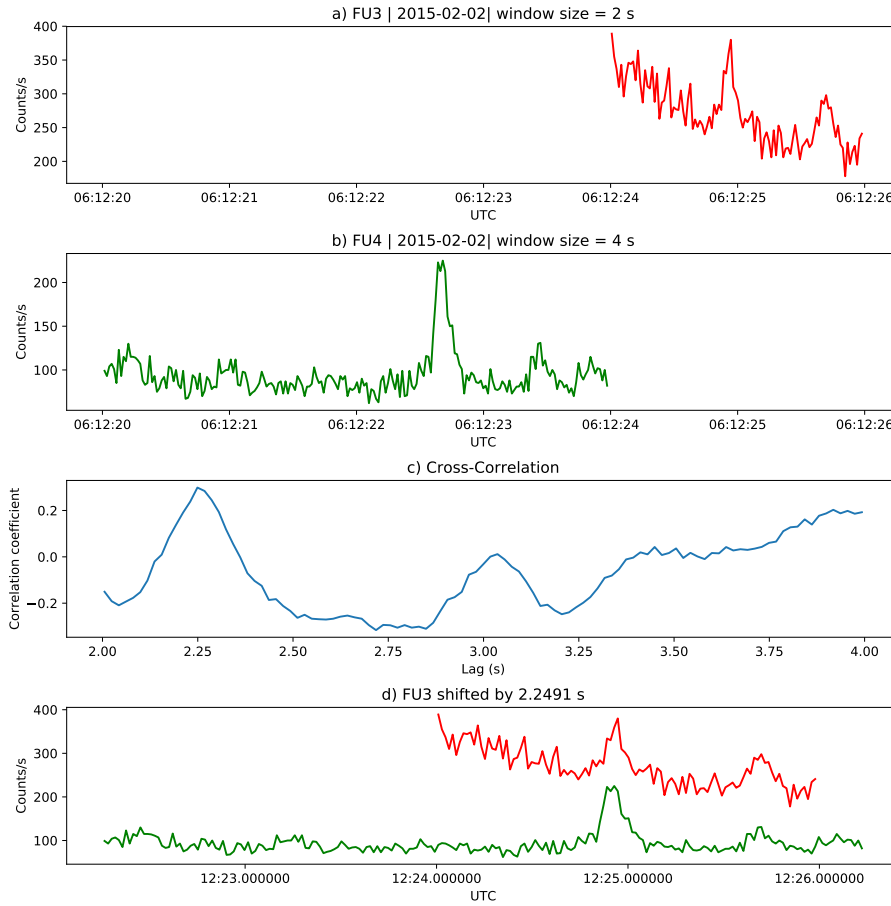


Figure A.3: Same analysis as Fig. A.1 on a different time period. Clock difference was 2.25 s.

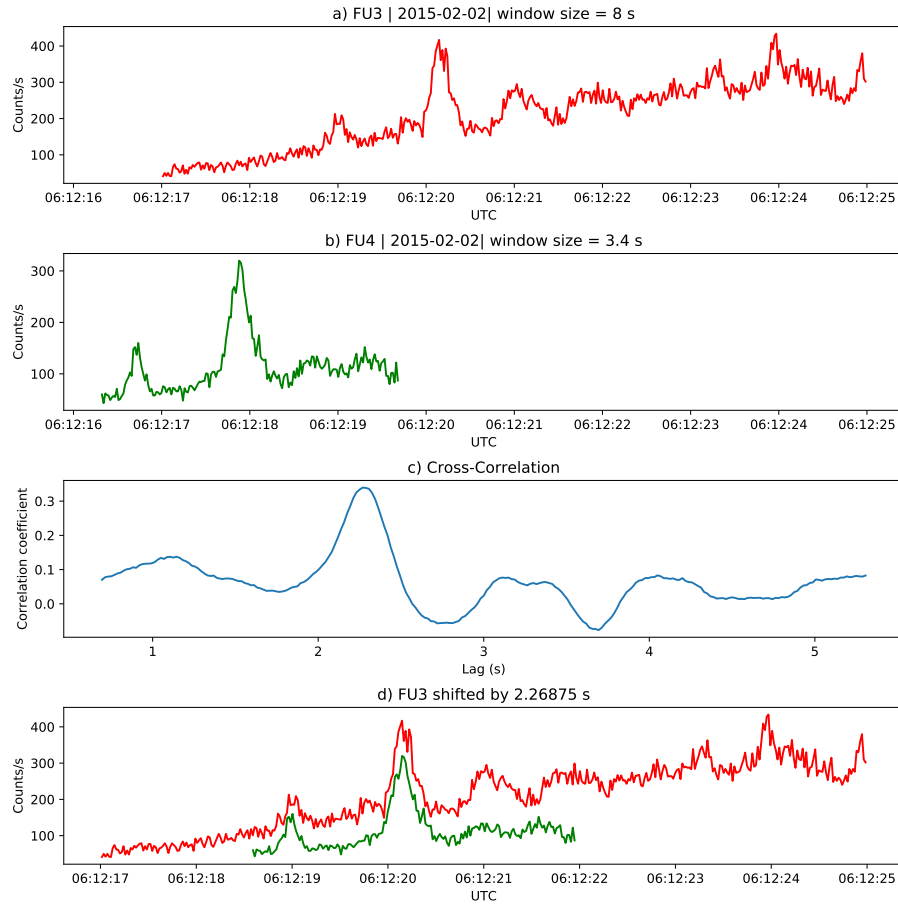


Figure A.4: Same analysis as Fig. A.1 on a different time period. Clock difference was 2.27 s.

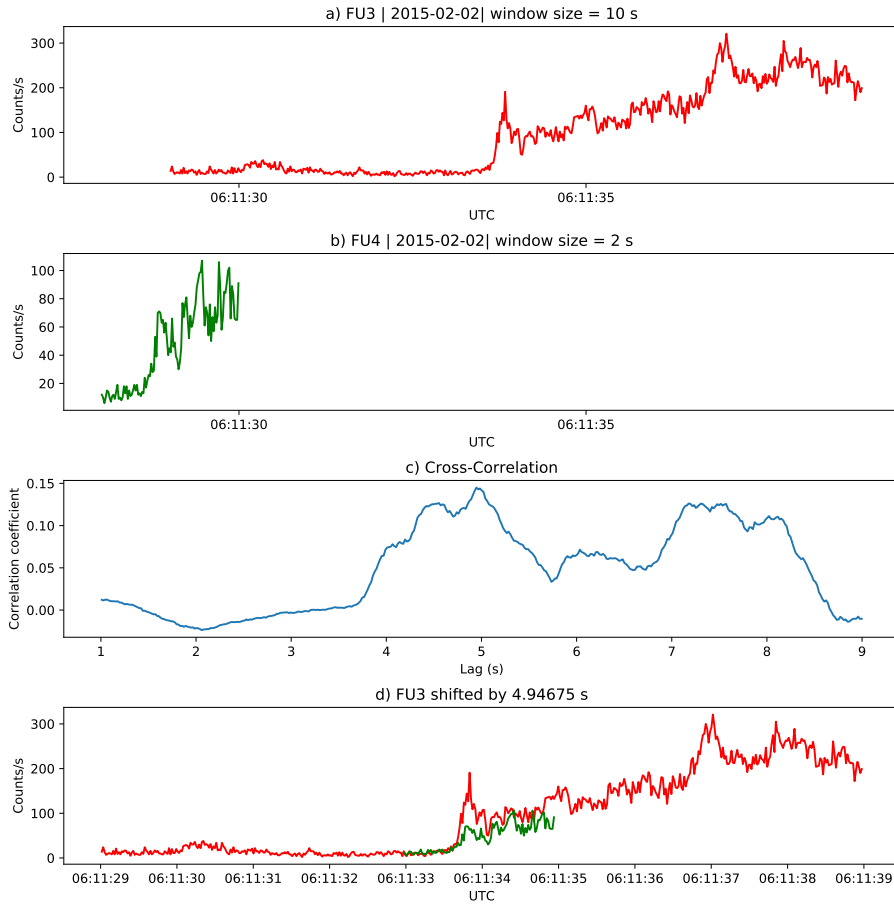


Figure A.5: Same cross-correlation time lag analysis applied to stationary spatial structures. The cross-correlation lag between these events is a sum of the clock difference and time lag due to the spacecraft separation. The lag derived at this time was 4.95 s.

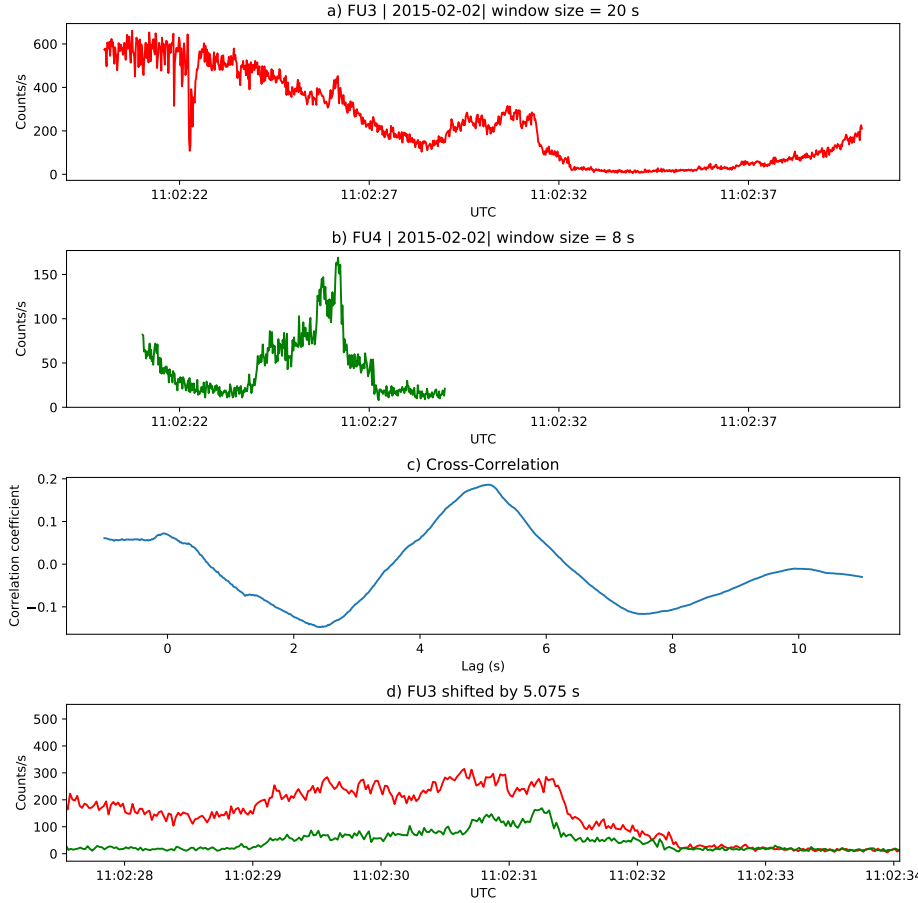


Figure A.6: Same analysis as Fig. A.5 applied to a different stationary spatial feature. The lag derived at this time was 5.01 s.